3D-modelling of fault-induced small-scale secondary fracturing in crystalline rocks

Justus Jokiniemi

Master's thesis

University of Turku

Department of Geography and Geology

Geology section

July 2021

University of Turku

Department of Geography and Geology, Geology section

JOKINIEMI, JUSTUS: 3D-modelling of fault-induced small-scale secondary fracturing in crystalline rocks

MSc thesis, 59 p + 4 appendices pp.

Bedrock geology

July 2021

The originality of this thesis has been checked in accordance with the University of Turku quality assurance system using the Turnitin OriginalityCheck service.

The objective of this Thesis was to develop new methods to model the microstructures within the bedrock, as these models improve the understanding of the properties of the micro-scale fracture networks and could be further applied to improve the interpretation of kinematics in the deformation zones and micro-scale hydrological properties of the different rock types. The second aim of the study was to compare datasets generated from the same samples by two alternative methods: X-ray Ct-scanning and the new 3D-grinding method. The study area is located in the municipality of Geta, in the northern parts of the Åland Islands, southern Finland. The Geta fault is a sub-vertical NE-SW trending dextral strike-slip fault. The 3D character of the fault and its well-developed damage zone allows studying the fault and its deformation zone in various scales and methods.

Setting for the 3D-samples was defined by field observations, 2D fracture and fault mapping from orthophotographs and 3D-photogrammetry models, which allow correlation of the 3D-fracture network characteristics in variable scales and with regional 2D-datasets from recent and ongoing investigations (Orrengrund and other MIRA-3D project targets).

3D-samples were drilled into 50*50/60mm sized drill cores for the 3D-grinder. Two of the 3D-samples were first Ct-scanned and grinded afterwards with 3D-grinder for making possible the micro-scale topology analyses in different sample depths and 3D-modelling on microstructures.

Results show that grinding tomography images are accurate and many different details can be viewed from them. The grinding tomography method allows generating data based on which microstructures can be modeled and observed with micrometer accuracy. The results of the 3D-modelling indicate that the orientations and dips of the micro-scale secondary fracturing corresponds to the macro-scale fracturing within the damage zones. However, fracture intersection affects the fracture geometries in micro-scale but not in larger scale. Micro-scale topology analyses show very little variations compared to macro-scale analyses.

Keywords: fault, fracture, fracture networks, geometry, damage zone, topology

TURUN YLIOPISTO

Maantieteen ja geologian laitos, geologian osasto

JOKINIEMI, JUSTUS: 3D-modelling of fault-induced small-scale secondary fracturing in crystalline rocks

Pro gradu -tutkielma, 59 s. + 4 liites.

Kallioperägeologia

Heinäkuu 2021

Tämän opinnäytetyön päätavoitteena oli kehittää uusia menetelmiä kallioperän mikrorakenteiden mallintamiseksi, koska nämä mallit antavat kattavamman käsityksen mikromittakaavan rakoverkostojen ominaisuuksista ja niitä voitaisiin soveltaa edelleen parantamaan deformaatiovyöhykkeiden kinematiikan tulkinnassa ja eri kivilajien mikromittakaavan hydrologisten ominaisuuksien ymmärtämisessä. Tutkimuksen toisena tavoitteena oli vertailla samoista näytteistä saatuja tietoaineistoja kahdella vaihtoehtoisella menetelmällä: X-ray CT-skannaus ja uusi 3D-hiontamenetelmä. Tutkimusalue sijaitsee Getan kunnassa, Ahvenanmaan pohjoisosassa. Getan siirros on kaateeltaan jyrkkä koillis-lounas suuntainen oikeakätinen kulku-siirros. Siirroksen 3D-luonne ja sen hyvin kehittynyt tuhoalue mahdollistavat siirroksen ja deformaatiovyöhykkeen tutkimisen eri menetelmillä.

3D-näytteet porattiin 50*50/60mm kokoisiksi kairasydämiksi 3D-hiomakonetta varten. Kaksi 3D-näytteistä skannattiin ensiksi CT-skannerilla, jonka jälkeen ne hiottiin 3D-hiomakoneella, mahdollistaen mikrorakenteiden 3D-mallintamisen ja mikromittakaavan topologia-analyysit eri näytesyvyyksiltä.

3D-näytteiden paikat määriteltiin kenttähavaintojen, ortokuvien ja 3D-fotogrammetria-mallien perusteella, jotka mahdollistavat 3D-rakoverkon ominaisuuksien vertailun eri mittakaavoissa ja alueellisten 2D-aineistojen kanssa viimeaikaisista ja meneillään olevista tutkimuksista (Orrengrund ja muut MIRA-3D projektin kohteet).

Tulokset osoittavat, että hiontatomografiakuvat ovat tarkkoja niistä voidaan tarkastella monia erilaisia yksityiskohtia. Hiontatomografiamenetelmä mahdollistaa datan tuottamisen, jonka perusteella mikrorakenteita voidaan havaita ja mallintaa mikrometrien tarkkuudella. 3D-mallinnuksen tulokset osoittavat, että mikromittakaavan sekundääristen rakojen suunnat ja kaateet vastaavat makromittakaavan rakosuuntia tuhoalueilla. Mikromittakaavassa rakojen leikkauspisteet näyttävät vaikuttavan rakojen geometrioihin, kun taas suuremmassa mittakaavassa vastaavaa vaikutusta ei ole havaittavissa. Mikromittakaavan topologia-analyysituloksissa on hyvin vähän vaihtelua verrattuna makromittakaavan analyysituloksiin.

Avainsanat: siirros, rako, rakoverkosto, geometria, tuhoalue, topologia

TABLE OF CONTENTS

Note: Third and fourth order headers are not displayed in the Table of Contents.

1 INTRODUCTION

Rock as a material is not intact but contains small micro-fractures that in suitable stress state may grow and eventually coalesce into larger fractures (Griffith, 1921; Griffith, 1924). This existing anisotropy of rocks provide nuclei for fracture growth and linkage to form faults (Cowie and Scholz, 1992). Griggs and Handin (1960) distinquish two modes of brittle failure; depending on the ratio between the orientations of micro-fractures and prevailing stress state and its magnitude, either *extension* or *shear* fracture is formed. According to the Griffith's theory, one of the distinctive features of rock mechanics is that shear fractures cannot extend in their own plane, yet their growth is initiated by Mode I extension fractures which form in tips of shear fractures. This phenomenon is caused by differences in rock strength between tensile and compressional stress states, as the tensile strength of the rock is considerably smaller than the compressional strength and hence fracturing rather occurs in extension than in compression (Scholz, 1989; Hoek and Brown, 1997). *Extension fracturing* takes place when the differential stress is relatively low and fractures generate perpendicular to the minimum ($\sigma 3$) and parallel to the maximum ($\sigma 1$) compressive stress, opened up at a high angle to the fracture plane (Griffith, 1924; Griggs and Handin, 1960). *Shear fracturing* takes place when the angle of the fracture relative to the maximum compressive principal stress is less than 45° and the relative displacement is parallel to the fracture surface (Griffith 1924; Griggs and Handin 1960). *Hybrid fractures* have characteristics of both extension and shear modes. They occur as a transition mode from tensile fracturing to shear fracturing; if the differential stress increases, shear component develops on a fracture surface, which has a relative angle of less than 30° to the $\sigma 1$ (Griffith, 1924; Hancock, 1985; Ramsay and Chester, 2004).

Strike-slip faulting is a common type of deformation and it occurs at many scales, under triaxial stress field. Strike-slip faulting is result of two blocks moving sideways, horizontally, parallel to the strike of the fault zone (e.g. Biddle and Christie-Blick, 1985). In the brittle regime, faults are initiated either from pre-existing structures, precursory structures (Crider and Peacock, 2004). As the fault initiates it gives a rise to development of subsidiary fracturing that are known to form synchronously with faulting (Paterson, 1978). These subsidiary fractures are commonly referred to as Riedel fractures or shears (Cloos, 1928; Riedel, 1929; Tchalenko, 1970). As faulting propagates, the repetitive

process of fault-induced subsidiary fracture growth leads to a damaged volume of fractured rocks around a fault surface with variable orientations and high frequencies compared to surrounding area (Pollard and Segall, 1987; Bilham and King, 1989; Sibson, 1989) known as fault damage zones (DZ) (Cowie and Scholz, 1992; McGrath and Davison 1995; Caine et al., 1996; Kim et al., 2004; Childs et al., 2009; Choi et al., 2016; Peacock et al., 2017). Rock volumes associated with increased fracture interaction and intersection are principal areas for stress concentration (Crider and Pollard, 1998) and similar areas play a large role in structural evolution (Kim et al., 2004) as existing fracture represents a plane of weakness. For this reason, sets of fractures are prone to be reactivated at the time of overprinting events (Peacock et al., 2018).

Kim et al., (2004) classified DZs into tip-, wall-, and linking-DZs based on how they are positioned around the faults. Tip DZ is a volume of deformation formed in response to stress concentration at a fault tip; wall damage zone is a volume of deformation caused by fault propagation either from damage corresponding with increase in the slip on the fault. A linking DZ is volume of deformed rock at a step between two sub-parallel and coeval faults (Kim et al., 2004). In addition to Kim et al., (2004), Peacock et., al (2017) added a new category in to the damage zone description called *interaction* DZ, which is further divided into *approaching*, *fault bend* and *intersecting* damage zones. Interaction DZ covers the districts where deformation is caused by kinematic and/or geometric linkage between two or several faults (Peacock et al., 2017). Consequently, damage zones can be used in determining fault propagation and how they are arrested (McGrath and Davison, 1995).

Brittle fault zones and fault-related structures are the most notable factors for fluid flow on any scale in crystalline bedrock as they form key controls (Caine et al., 1996) by providing opportunities for fluids and gasses to reach the formed cavities (Anders, 2014) by introducing highly conductive pathways or either form barriers to flow in fault systems (Nelson, 2001). Fracture networks also control many of the physical properties of rocks such as permeability, porosity and strength (Sanderson and Nixon, 2015). Connectivity and properties of fracture networks can be characterized using the topology. Topology is a mathematical term applied to 2D fracture networks, it characterizes which of the fractures intersect each another, which abut against other fractures and which occur in isolation (e.g. Sanderson and Nixon, 2015). Characterization by topology includes usage of nodes and branches, which are dependent on geometry and topology of the fractures (Manzocchi, 2002; Sanderson and Nixon, 2015) in addition dimensional parameters that

are invariable to scale, strain and continuous variations (Jing and Stephansson, 1997). Topology of two-dimensional fracture network consists of traces, nodes and branches, where each trace comprises of one or more branches with a node at both ends of the trace. 2D topology consists of three types of recognizable nodes; intersection point between two crossing traces, forming an X pattern (X-node), trace ends at another trace, forming a Y pattern and isolated trace (I-node) (Manzocchi, 2002; Sanderson and Nixon, 2015). Node quantities allow to subsequently determine the fracture network (Manzocchi, 2002). In three-dimensions fracture set comprises of a limited number of surfaces or planes, which either intersect with other planes at intersection or they terminate at tip line (Sanderson and Nixon, 2015).

Knowledge of the properties of fractures has numerous applications in science and engineering, as they provide information on the history of the brittle deformation zones, thus they imply the kinematics and age relations of the parent faults (Kranz, 1983; Bastesen and Rotevatn, 2012). Yet the knowledge of the 3D-geometry of fracture networks has uncertainties regarding to various details e.g. fracture connectivity, interaction and scaling. From engineering aspect, the understanding of micromechanics (propagation and interaction of fractures) of fracturing becomes important when considering the stability of the bedrock in the underground openings and predictions of hydrological permeability of the damaged rocks (Nasseri et al., 2011). Along with the Finnish government's recent plans for utilizing the Precambrian bedrock for repository of nuclear fuels, the fracturing is also a critical factor for making pathways for radionuclides in underground nuclear waste repository facilities (Laubach et al., 2019; Siren et al., 2015).

The studied geological features are always three-dimensional and covering fault and fault-related comprehensive geometric 3D-architecture is therefore of primary importance for fully understanding properties of such structures and how they are arrested. Despite of the importance of recognizing the complete geometric architecture, the published studies over 3D secondary fracturing still remain relatively few. Fault-induced damage zone fracturing has been widely studied in 2D (Kim et al., 2004; Choi et al., 2016; Peacock et al. 2017) which may be used as a proxy for the 3D distribution of damaged rock volume around the faults. However, the ideas are still mainly driven by interpretations based on 2D-data. Field observations and further studies related to secondary fracturing and fracture network connectivity are also based widely on 1D and 2D, which is problematic when trying to understand the fracture density and connectivity

on three-dimensions. Three-dimensional data of the structural geometries of fracture networks relies often on individual exposure surfaces and on 3D seismic data (Barnett et al., 1987; Berkowitz 2002).

Despite the limitations on the study the 3D-architecture of the fracture networks, some research has also been done in 3D. For example, Crider and Pollard (1998) and Martel et al. (2001) have constructed a 3D-geomechanical model of mechanical interactions and local stress perturbation in secondary fault developments, whereas Martel and Boger (1998) have studied the "geometry and mechanics of secondary fracturing around small three-dimensional faults in granitic rock" using field measurements in addition to mechanical modelling. Modelling based on laboratory experiments also includes e.g. Nasseri et al. (2011) who used the x-ray CT-scanning method to visualize the development of secondary micro-fractures in anisotropic granite. These numerical methods (Crider and Pollard, 1998; Martel and Boger, 1998, Gillespie and Pollard, 2002) and laboratory experiments (Nasseri et al., 2011) can provide comparable models for examples found in nature. The problem, however, is that detailed models of 3D-geometry of naturally occurring secondary fracturing have not been previously made, or the existing studies do not appropriately take into account the structural setting of the sample, particularly their spatial occurrence with respect to the contrasting types of the fault DZs. For instance, strike orientations of secondary fractures have been discussed in many articles, yet information on characteristic dip-angles of the secondary fractures is difficult to find. Based on the field observations by Martel and Boger (1998), the predominant dip-angles of secondary fractures in crystalline granite are steeper than 80°. However, recent fieldwork in the Orrengrund Island, Loviisa, southern Finland, has shown inconsistency with these results; wing-crack type secondary fractures in crystalline rapakivi granite have been found to have gentler dips than expected (Skyttä et al., 2021). The reasons for the differences are probably related to rock mechanics and prevailed paleo-stress field, but even comparing the results would require development of better methods to study the 3D geometry of secondary fractures.

The first aim of this Thesis is to generate 3D-models over fracture networks associated with faults and their deformation zones occurring in crystalline rocks and evaluate the relationship between faults and fault-related secondary fracturing and fault kinematics. The second objective of the work is to compare the datasets generated from the same samples by two alternative methods: X-ray Ct scanning and the new 3D-grinding method. This investigation further aims at investigating scalability, particularly significant would

be if the results can be scaled, as more regional investigations miss the 3rd dimension, which is provided by this study. For these purposes, six samples were taken and analyzed from contrasting damage zones associated with a sub-vertical Geta strike-slip fault, Åland, which transects mesoscopically isotropic Rapakivi granites. The setting for the 3D-samples is defined by field observations, 2D fracture and fault mapping from orthophotographs and 3D-photogrammetry models, which allow correlation of the 3D-fracture network characteristics in variable scales, and with regional 2D-datasets from recent and ongoing investigations (Orrengrund and other MIRA-3D project targets).

The following points are of particular significance to meet the goals of this study:

i. Development of the automatized grinding tomography method to construct detailed models of 3D micro-fracture networks within natural rocks.

ii. Determination of characteristic 3D-geometry of secondary micro-fractures within early-stage faulting in crystalline rocks.

iii. Unravel how the 2D models of the fracture networks correlate with the created 3D models of secondary micro-fractures, and how this information can enhance the interpretation of fault kinematics and properties of the damaged rock volume.

iv. Utilizing digital photogrammetry in 3D model with fault, DZ and variation in these selection of sample sites structural interpretation and analysis.

v. Discuss the critical topic areas of future development such as artificial intelligence assisted image pattern recognition in grinding tomography data processing topology of fracture networks.

The Thesis was conducted under MIRA-3D -project (microstructures-3D) of the University of Turku funded by Valtion Ydinjätehuoltorahasto (VYR). The MIRA-3D-project aims to develop new methods to model the micro-fractures within in the bedrock. These models provide a wider understanding of the properties of the micro-scale fracture networks (e.g. 3D-geometry), and therefore, could be applied to improve the

interpretation of kinematics in the deformation zones, and micro-scale hydrological properties of the different rock types. The project applies the 2D-topology analysis methodology used in the KARIKKO-project, of which main aim was to study scalability of fracturing in the bedrock; if the compared intensity and lengths distributions of fracture trace data follows the same distributions in different scales, this information can be used for predicting the connectivity of fracturing in study areas with no bedrock exposures (Bonnet et al., 2001).

1.1 FRACTURES

1.1.1 Fractures

The term *fracture* covers many different structures such as joints, veins, dykes, faults, and deformation bands (Schulz and Fossen, 2008). Fracture is any planar either sub-planar discontinuity that has two parallel surfaces which encounter at the fracture front (Pollard and Segall, 1987). Fractures characterize discontinuities in displacements where the rocks or minerals are scattered due to the loss of cohesion along the weakest plane of the rock, caused by external or internal stress (Fossen, 2010). Groups of individual fractures either sets of fractures form a fracture network, where fractures intersect at intersection points or intersection lines (Sanderson and Nixon, 2015; Peacock et al., 2018) and are characterized by their connectivity and by many varied geometrical distributions, such as location, orientation, length, density, and aperture (Berkowitz, 2002). At its simplest, networks may consist solely of a single fracture set or they may comprise numerous sets with variable orientations with combinations of different fracture types, each type having its own effects on a rock volume (Peacock et al., 2016; Peacock et al., 2018). Fracture networks may have formed in unique deformation events, when they are most likely kinematically linked but they may also form in series of events under variable conditions and it is also likely for a fracture set to be reactivated at the time of subsequent events (Peacock et al., 2018). Evaluating the properties of rock-mass effected by active fracture set, requires analysis of individual fractures as well as the fracture network.

1.1.2 Subsidiary fracturing

Riedel shear structures (Cloos, 1928; Riedel, 1929) are patterns of shear bands, symbolized by R and R', also referred as Riedel shears (R) and conjugate Riedel shears (R') (Hills, 1963; Tchalenko, 1970). The R shears generally develop as first subsidiary fractures during early stages of faulting, propagating out of main fault and being coeval with it (Tchalenko, 1970) (Fig. 1). R-shears are displayed at an acute angle (10-20°)

clockwise (dextral) either anticlockwise (sinistral) often as *en échelon* arrays as synthetic to the sense of slip across the main fault, and therefore used for interpretation of faults kinematic evolution (Tchalenko, 1970). Distribution, surface strike orientations, dips and lengths of early Riedel shears may differ depending on several factors such as, initial stress state and complexity of the basement fault configuration. With increasing displacement, Riedel shear tips may accommodate short-lived splay faults, leading to the emergence of small-angled Riedel and P shears that link and interfere with the Riedel shears. R' shear fractures are antithetic, orienting at high angle 75-90° towards main fault, developing simultaneously or after R shears (Tchalenko and Ambraseys, 1970). Moreover, R' shears tend to connect overlapping R shears by occurring in the overlap zone between two parallel R shears. As the Riedel system develops progressively, the P-shears may form as result of alteration of the incremental strain field, however occurring less often than R and R' shears, as they may need larger displacement to form (Tchalenko, 1970; Naylor et al., 1986; Sylvester, 1988). P shears are associated with R shears in approximately symmetrical angles with respect to fault plane (Tchalenko, 1970). In addition to inclination, they also form *en echelon* array synchronous with R shears. P shears are contractional, as shearing propagates, P shears accommodate fault parallel shorterning. There is possibility for P' shears conjugate with P shears, however there are difficulties in dividing them in terms of orientation from R' shears. T-fractures (= extension fractures) form at the same time, as the R fractures, yet in larger angle of 45° with respect to the fault and occasionally they may form instead of R fractures (Tchalenko and Ambraseys, 1970). Last to form are Y shears, which are synthetic microfractures sub-parallel to the main fault. In case of a narrow fault zone with bulk borders parallel to the main fault, Y shears may all be connected and form anastomosing fracture network (Woodcock and Schubert, 1994).

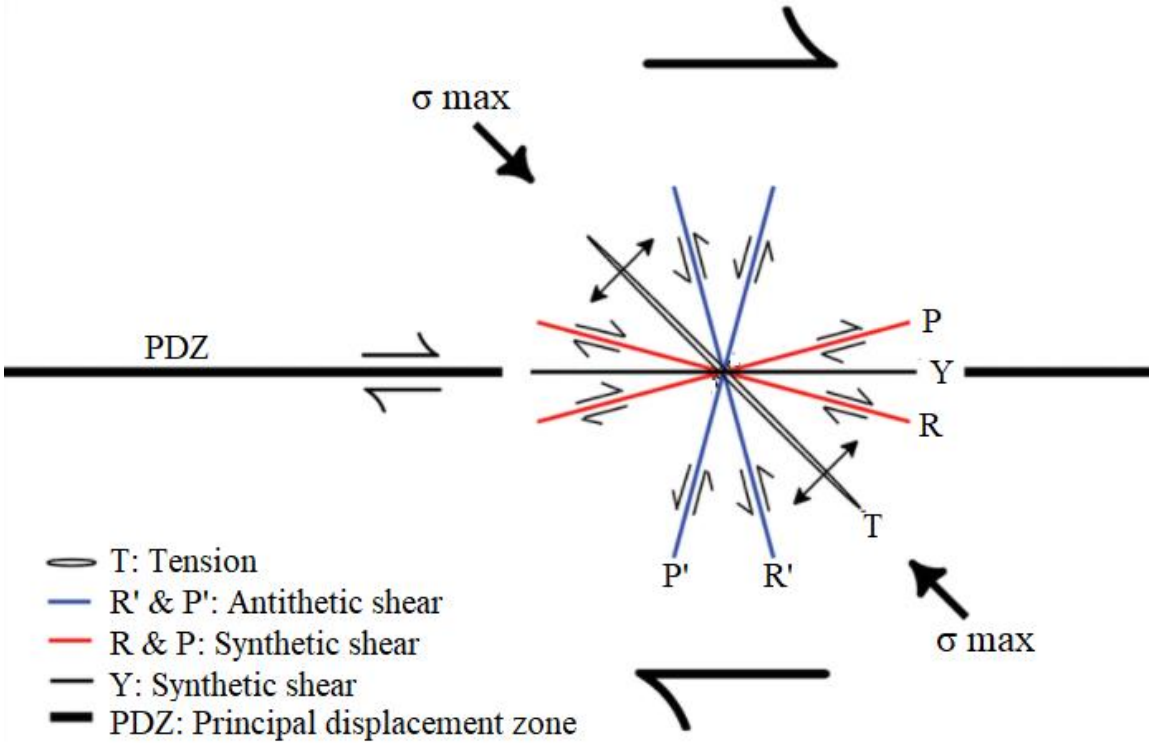

Figure 1: Illustration of an idealized subsidiary fracturing (Cloos, 1928; Riedel, 1929; Tchalenko, 1970). Figure modified from Xu and Ben-Zion (2013).

1.1.3 Wing-cracks and horsetail fractures

Wing-cracks are tensile mode I cracks (Brace and Bombolakis, 1963; Lajtai, 1971) they form in uniaxial compressive conditions thus, which may also form in tensional stresses caused by high pore pressure conditions (McGrath and Davison, 1995), or under low effective stresses (Kim, 2000). Due to their opening-mode genesis, wing-cracks are frequently filled with hydrothermal mineral assemblages which indicates their importance for the subsurface fluid flow (Mutlu and Pollard, 2008). Wing-cracks form as high angle cracks at one or both ends of shear fracture. Instead of propagating on their own plane, they start at the tips of the pre-existing fracture (Fig. 2), such as fault for example (Brace et al., 1966; Cruikshank et al., 1991; Bobet 2000).

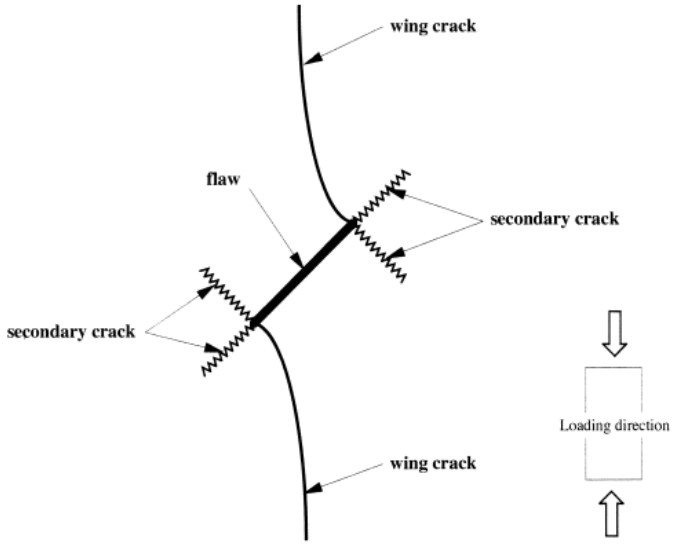

Figure 2: Simplified illustration of wing-crack forming pattern in uniaxial compression. Figure after Bobet (2000).

2D laboratory experiments and theoretical studies suggest that wing-cracks tend to propagate from the tip of the flaw and curve towards the orientation parallel to direction of σ1 compressive stress, occurring in situations where tip of the pre-existing flaw undergoes sudden changes in frictional strength (Brace and Bombolakis, 1963; Lajtai, 1971; Horii and Nemat-Nasser, 1986; Pollard and Segall, 1987; Petit and Barquins, 1988), where the propagation towards σ1 is kinematically caused by cracks opening by its sliding sides or contact area (Dyskin et al., 1999). In order to lengthen the wing-crack, increase in compression is necessary (Bobet 2000). However, 3D experiments made my Dyskin et al. (1999) shows that wing-crack growth has certain limits; size of a wing is at maximum the same size as the parent flaw.

Horsetail and/or pinnate fractures (Granier, 1985; Petit and Barquins, 1988) corresponds geometrically and mechanically to the wing cracks but are characterized by a rather smaller angle to the main fault (Granier, 1985; Hancock, 1985; Petit and Barquins, 1988; Engelder, 1989; Kim et al., 2004). These structures occur in dilatant zones of the faults, where the fault slip undergoes dilatation (Granier, 1985) forming in biaxial conditions (Petit and Barquins, 1988). Horsetail fractures have tendency to fade out more gradually towards the plane tip compared to wing-cracks (Kim et al., 2000) and they may also be reactivated as synthetic faults during later deformation stages (Granier, 1985; Kim et al., 2001). Wing-crack and horsetail fractures are both generated as mode I fractures, even though horsetail fractures are asymmetrically arranged with respect to the initial flaw (Brace and Bombolakis, 1963; Pollard and Segall, 1987; Fossen, 2010).

1.2 DAMAGE ZONES

Brittle faults can be divided into two principal components: fault core and the surrounding *damage zone* (DZ). DZ differs from the surrounding wall rock volume by rather dense fracture frequencies and variable fracture orientations compared to surrounding host rock (Chester and Logan, 1986; Ishii, 2016). Damage zone has been generated initiated by propagation, interaction, and build-up of slip along the fault (Cowie and Scholz, 1992; McGrath and Davison 1995; Caine et al., 1996; Kim et al., 2004; Childs et al., 2009; Choi et al., 2016; Peacock et al., 2017). Compared to fault core, DZs are characterized by comparatively lower strain and less intense deformation (Billi et al., 2003) but display characteristic secondary fracturing (Martel et al., 1998) showing a broad variety of geometries and fracture patterns (Kim et al., 2004); as faulting occurs, the geometrical irregularities affect one of the other, causing stress concentration to form additional fractures in the surrounding rock volume with variable orientations and fracture patterns compared those formed in the slip zone (Chester and Chester, 2000; Wilson et al., 2003; Faulkner et al., 2011). There are several different factors that may control the character of DZs around faults, the most notable factor is the fault initiation style, which ultimately controls the primary fault-rock characteristics (Crider and Peacock, 2004). Other affecting factors are variations in lithology, rheology, orientation of cleavage or bedding relative to the slip direction of the fault, and the affecting stress system, location, slip mode and developmental stage of the fault (Kim et al., 2004).

Previously DZs have been classified according to their positions at fault tips, slip surface "walls" or areas of linkage (tip, wall and linking DZs; Kim et al., 2004.) but they have been subsequently reclassified (Choi et al., 2016; Peacock et al., 2017). Kim et al. (2004) classified damage zones as follows: *Tip* damage zone is the area of deformed rock volume around the fault tips, formed in response to stress concentrated at a tip of fault. Particularly strike-slip faults show a variety of DZ-structures around the tip, such as two different modes around strike-slip fault tip lines; mode II when tip is lateral and mode III occurs at up- and down-dip tips, mixed slips between mode II and mode III are also possible, typically shown as wing-cracks, horsetail fractures, synthetic either antithetic fault or mixed variables between aforementioned types (Kim et al., 2004; Peacock et al., 2017). Fault *splays* or *branches* often show linkage with the main fault, since they form with the same sense of slip and have same orientation (Kim et al., 2004) while the *antithetic* faults show opposite orientation compared to main fault, for them it is common that they show an increased length and spacing away from the fault tip (Kim and Sanderson, 2006). *Wall*

damage zone covers a volume of deformation caused by propagation of faults or from damage associated with increased in slip on a fault, typically occurring as *en echelon* arrays or extension fractures (Kim et al., 2004). Wall DZ may be distributed along the whole trace of a fault. In these cases, the damage is resulting both from the termination of tip DZ and development of new structures in the fault walls (Kim et al., 2004). *Linking* DZ occurs as a step between intersecting sub-parallel faults, evolving between two interacting coeval sub-parallel faults as result of spacing problems, hence linking DZs may occur either as contractional step or extensional step (Fig. 3) often characterized by intense fracturing (Kim et al., 2004). Occasionally it may be difficult to distinguish them from tip DZs as they occur around the fault tips together with tip damage (Kim et al., 2004; Peacock et al., 2017) and therefore, should be only characterized as linking DZ, when associated with clear evidence for the presence of two separate fault segments.

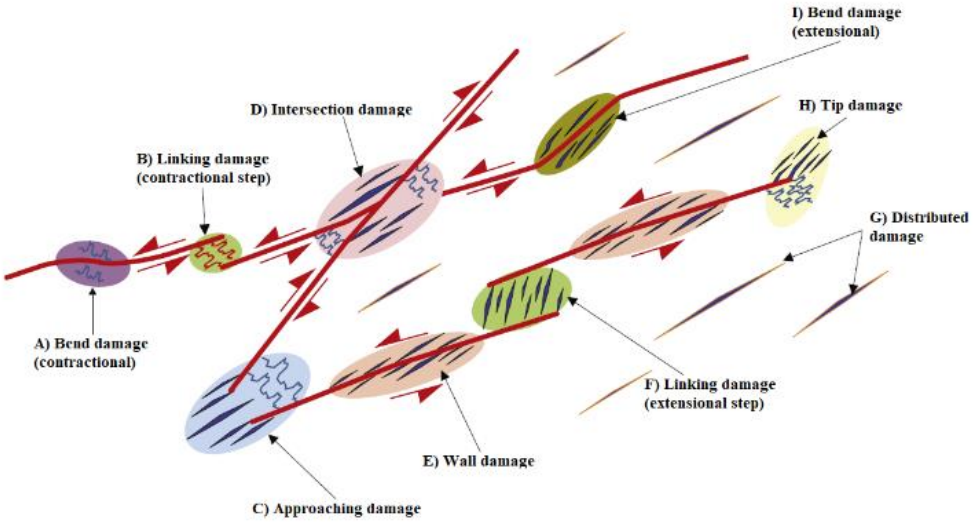

Figure 3: Different types of damage zones described by Kim et al., (2004) and Peacock et al., (2017). Figure after Peacock et al. (2017).

Due to the above uncertainties in DZ classification, a more comprehensive definition is useful because it covers a wider range of fault relationships, such as interaction between faults, irrespective of their relative orientation or age (Peacock et al., 2017). With the broader usage of DZ concept, the role of post-fault deformation, mineralization and stresses is more convenient, for example predicting fluid flow related to fault interaction (Peacock et al., 2017).

Peacock et al. (2017) describes the new category of *interaction* DZs, which come in play when two or several faults approach each other and interact kinematically. Interaction DZ is further divided into *intersection*, *approaching* and *fault bend* damage zones (Peacock

et al., 2017). *Intersection* DZ comprises of deformation around either point or line of intersection of two or more faults for example, abutting or cross-cutting each other, which makes faults in question geometrically linked, but they are not necessarily linked kinematically (Peacock et al., 2017). In *approaching* DZs faults do not intersect and are not geometrically linked, however, they are linked kinematically and their displacements influence each another (Peacock et al., 2017). *Fault bend* DZs consist of areas around a bend on a fault (Peacock et al., 2017) displacement being either extensional (Kurt et al., 2013) or compressional (Janecke et al., 2010). Occasionally fault bend DZs may represent former linkage points, making it difficult to determine causes of certain bends along faults (Peacock et al., 2017). Peacock et al. (2017) also uses term *distributed* damage zone referring to how the precursory fault damage is distributed to an area or zone, where the deformation is more intense compared to the surrounding area. Usage of these new definitions can cause uncertainties, especially in areas with limited exposure surfaces, where the faults that seem unconnected to each other, they may be actually linked geometrically under the surface, where this linkage cannot be observed (Rotevatn and Fossen, 2011; Peacock et al., 2017). DZs play an important role in many geological subjects, such as fluid permeability in the crust (Caine et al., 1996) which is exploited in several practical applications related to ore-deposits (Brogi, 2011) hydrocarbon reservoirs (Aydin, 2000) and ground water (Lopez and Smith, 1995). DZs can also be further assessed together with fault initiation and propagation, in order to recognize regional strain distribution (Scholz and Cowie, 1990; Crider and Peacock, 2004) and for example, predicting progress of earthquake rupturing (Kim and Sanderson, 2008).

1.2.1 Permeability and fluid low within fault zones

Faults and fault-related secondary fracturing and their characteristics are the most prominent factors for fluid flow on any scale in low porosity rocks, such as crystalline basement of Fennoscandia, as they provide porosity and connectivity (Faulkner et al., 2010). Other affecting properties of fractured rock in fluid flow are fracture infill and its behavior within in situ stress conditions (Ito and Zoback, 2000) and thermo-hydro-mechanical-chemical properties of the host rock. Furthermore, fracture interaction is a significant factor to consider when assessing hydraulic fracture propagation in naturally fractured formations, since interaction between these two is likely to affect permeability by forming complex fracture network (Weng et al., 2011).

Considering the hydraulic behavior of the fault zones, both the main slip zone and the damage zone should be notified (Caine and Forster, 1999) as they form key controls on fluid flow in upper-crustal brittle fault zones (Caine et al., 1996) either as fluid conduits or barriers (McCaig, 1988). The fault zone permeability displays variations between the fault core and damage zone: e.g. core permeability is influenced by grain-scale permeability of fault rock and damage zone permeability is strictly dependent on the hydraulic properties of the fracture networks, as a result permeability between fault zone and wall rock also varies considerably (Caine et al., 1996), particularly in crystalline rocks due to fact that permeability inflicted by fractures is considerably higher than permeability of intact crystalline host rock (Mitchell and Faulkner, 2008). As Achtziger-Zupancic et al., (2016) study shows, majority of the transmissivity is produced within nearest 30% to 50% of the fault damage zone, and the cumulative flow tends to decrease exponentially from the fault zone toward the host-rock as the fracture frequency is decreased. The permeability properties may alter over geological time, or in a timescale relevant to industrial applications (D.R. Faulkner et al., 2010), which must be considered when applying knowledge of fluid flow properties within industrial applications (Lunn et al., 2008) such as nuclear waste repository (Fox et al., 2012).

1.3 MICRO-FRACTURING PROCESSES IN CRYSTALLINE ROCKS

1.3.1 Morphological classification of micro-fractures

Observing crystalline rocks in grain-scale has confirmed that faults initiate and grow troughout the interaction of discontinuities (Crider, 2015). These discontinuities are mostly pre-existing micro-fracture networks and cleavage surfaces defined by platy mineral grains, and play significant role in initiation of faulting. The micro-fractures found in rocks tend to have high variety and complexity, which makes statististical studies alone difficult to describe the morphology of the micro-cracks (Kranz, 1983). However, Kranz (1983) has divided the micro-cracks into four basic types found from observations, which will be shortly described.

Grain boundary cracks are cracks associated with individual grains in the rocks (Kranz, 1983). The relationship with the crack and the grain boundary is not always obvious, thus the grain boundary cracks can be divided into *non-coincident* and *coincident* grain boundary cracks (Kranz, 1983). The non-coincident grain boundary cracks represent the situation when the crack probagating outside the boundary enters into the grain in low to

high angle to the grain boundary. The coincident grain boundary cracks, in turn represent the opening of space between the individual grain and the surroundin matrix material.

In thermally or mechanically stressed rock, the coincident grain boundary cracks connect through several grains. These fractures are called *intercrystalline cracks* or *transgranular cracks* (Kranz, 1983), which are relatively small cracks with length smaller than grain size and with $< 1\ \mu m$ aperture. *Intercrystalline* cracks found in rocks are usually mechanically or thermally induced, for which the characteristic features are sharp walls and tips. Mode I is typical type for intercrystalline cracks, and they usually form in extension with minor shearing on fracture plane. In 3D, the size can be twisted and tilted instead of forming perfectly planar surfaces (Kranz, 1983).

The *cleavage cracks* should be treated as completely separate group of micro-cracks as they are defined as separations along cleavage planes in minerals (Kranz, 1983). Several cleavage planes may occur within one mineral.

1.3.2 Generation mechanisms of micro-fractures

As the interaction of micro-fractures plays an important role in the initiation of faulting in crystalline rock (Crider, 2015), its also important to understand the physical prossesses behind the formation of such fracturing. According to Kranz (1983), the studies in natural and experimental conditions show seven mechanisms driving the formation of mechanically or thermally induced cracks in rocks:

1. **Twin lamellae cracking on grain boundaries**; e.g. crack nucleation in calcite twin lamellae.
2. **Strain energy relaxation of deformation lamellae**; kink band boundaries and discontinuity arrays cause compressional or extensional strains. This strain can be released thus causing the nucleation of micro-crack.
3. **Cleavage separation**; e.g. cracking in biotite through the plane of lowest atomic bond strength.
4. **Concentration of stress in neigbouring grain boundaries and cracks**; changes in stress field due to cavities in rock.
5. **Rotation and translation of grains**; deviatoric stresses can lead to grain boundary sliding, thus causing rotations of grains. This can happen e.g. in cataclastic deformation.

6. **Elastic compliance contrast in neighbouring grains and matrix**; boundary tractions generate under stress due to different mechanical properties in interlocked mineral grains.
7. **Thermally induced micro-cracking**; differential thermal expansion of rock mass leading to generation of tensile stresses. This mechanism plays dominant role in crack initiation mechanisms in granite due to differing thermoelastic modulus of quartz and k-feldspar.

Figure 4 shows some of the previously discussed micro-crack types situated with fault initiation modeling by Crider (2015). The modeling is done based on uniaxial compression tests for crystalline rock samples. Three experimentally conducted fault initiation models are presented: Figure 4a (i-iii) shows application of uniaxial compression on Chelmsford granite sample. The stress is applied parallel to a set of closely spaced cracks, which have lenghtened in “rifting” direction. As the strains increase, the cracks form columns which eventually buckle, thus forming continuous micro-fault with rough surface. In Figure 4b (i-iii), the fault is formed in Four-mile gneiss sample trough interaction of grain boundary cracks, which connect with intercrystalline cracks. Here the anisotropy of the rock plays a significant role. Moreover, in the last experiment on Westerly granite in Figure 4c (i-iii), the initial fractures nucleate within a so called *process zone*, where Mode I cracks are connected by concrentrated stresses on probagating Mode III shear fracture tips. Lenghtening of this process zone represents the fault probagation through the rock mass.

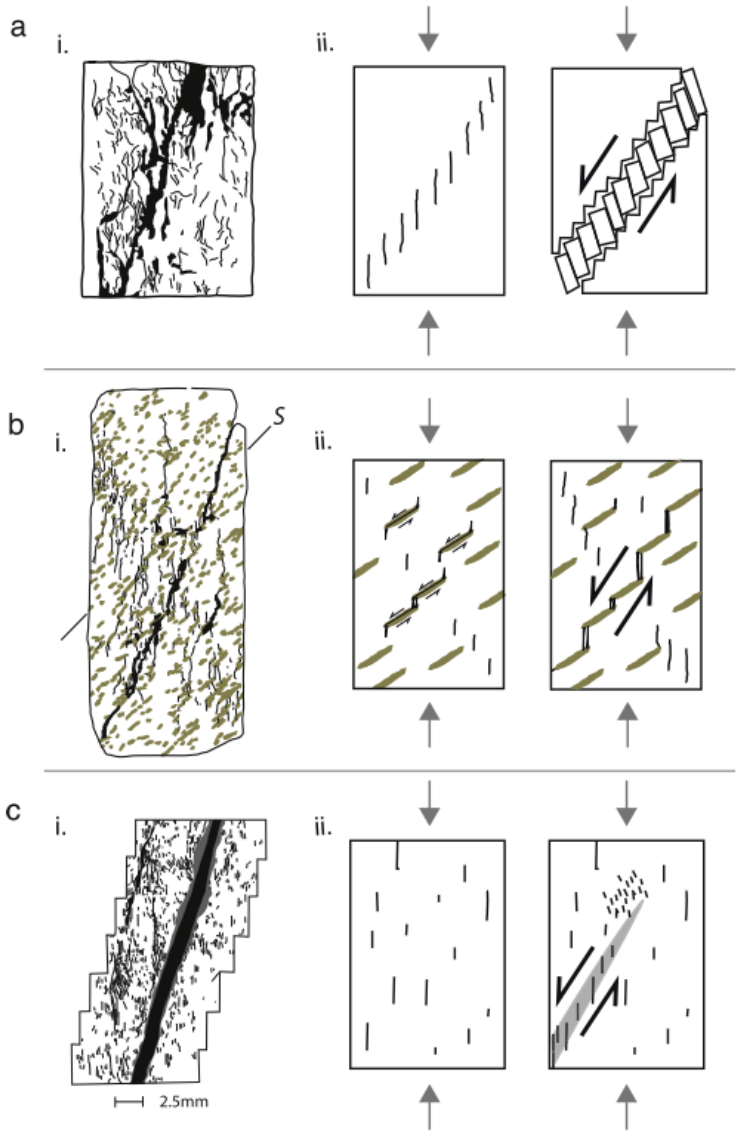

Figure 4: Illustrative picture of Chelmsford granite (a), Four-mile gneiss (b), and Westerly granite (c) presenting the sketched fracture patterns after uniaxial compression of rock sample (i). In addition, conceptual models of fault initiation (iii) are shown with nucleation cracks (ii). According to presented models, fault can initiate through grain rotation (a; iii), grain boundary crack linkage (b; iii) or tail-crack development (c; iii). Figure after Crider (2015).

2 MATERIALS AND METHODS

2.1 GEOLOGICAL BACKGROUND

Significant anorogenic event took place in mid-Proterozoic (1.67-1.47 Ga) forming Rapakivi granites and diabase dyke swarms in response to mantle upwelling and extension (Haapala and Rämö, 1990). Rapakivi granite melts formed in the deep parts of the continental crust and afterwards intruded into upper parts (Rämö and Haapala, 2005) this event was presumably controlled by the spatial distribution of earlier formed listric shear zones, faults and their interaction with the stress orientation, in this case within an extensional regime (Korja and Heikkinen, 1995). The extensional environment of Rapakivi emplacement is further corroborated by the diabase dyke swarms, which date back to same anorogenic event (Korja and Heikkinen, 1995; Rämö and Haapala, 1995; Nironen, 1997). The rapakivi granites occur as relatively thin 5 – 10 km thick sheet-like intrusives within the upper parts of continental crust (Korja and Elo 1993).

2.1.1 Post-1.6 Ga paleo-stress field and related brittle structures in Southern Finland

Research on brittle deformation evolution in Southern Finland has been implemented mainly in association with site investigations for a deep repository of high-level nuclear fuel in Olkiluoto area, southwestern Finland. Investigations in the Olkiluoto area has provided extensive fault-slip data sets derived from various sources such as repository tunnels, oriented diamond drill cores, and outcrops within the region. Based on these datasets, Mattila and Viola (2014) have constructed a conceptual model of brittle evolution from Paleoproterozoic Svecofennian orogenic events to Mesoproterozoic Sveconorweigian orogeny using computed paleo-stress tensor analysis and K/Ar -fault gouge age determinations (Viola et al., 2011). The model is divided into 7 stages (Fig. 5), of which stages 4-7 represent the post-rapakivi paleostress states after the 1.65 - 1.55 Ga Gothian orogenic event.

Paleo-stress analysis of Olkiluoto fault slip data on rapakivi granites and 1.27 Ga diabase dykes has shown two major compressional stress tensors. Stage 5 at around 1.2 Ga, after the emplacement of Rapakivi intrusions is represented by NNE-SSW -oriented compressional stress tensor. Furthermore, the orientation of the compressional stress tensor turned into opposing WNW-ESE orientation in Stage 6. Stage 7, in turn, implies an extensional tectonic event in the E-W direction. Based on documentation in SE

Norway and SW Sweden, the timing of this deformation seems to be synchronous with the stress regime of the 1.1 Ga Sveconorwegian orogenic event (Viola et al., 2011).

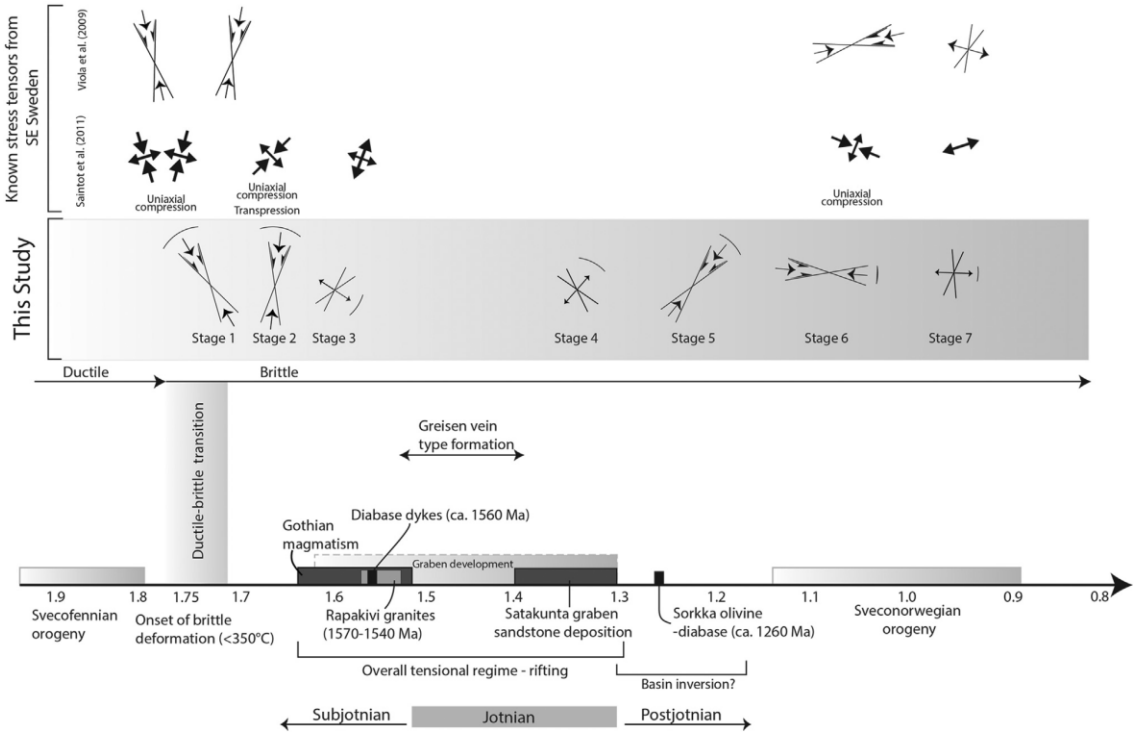

Figure 5: Model of the evolution of brittle structures in southwestern Finland constructed by Mattila and Viola (2014)

2.2 STUDY AREA

Intrusion of the Rapakivi granites was the last major geological event that affected the bedrock in Finland since Svecofennian orogeny (Nironen, 1997). This means that the brittle deformation structures have not been controlled by pre-existing anisotropy of the rock, thus, making the rapakivi granite optimal rock type for studying the early-stage brittle deformation structures. Åland Rapakivi batholith is the second largest rapakivi batholith in Finland, covering approximately 5000km^2 area (Ehlers and Bergman, 1984; Karell et al., 2014) its emplacement happened during the late stages of this magmatic event in N-S trending extensional tectonic setting (Vaasjoki et al., 1991; Nironen, 1997; Rämö and Haapala, 2005). Åland Rapakivi batholith comprises of multiple different type granites, which also represent different stages of different melt crystalline phases, in total six different plutonic rocks have been recognized from Åland rapakivi batholith although majority of the lithology consists of Wiborgite and Pyterlite (Bergman, 1981; Karell et al., 2014).

The study area is located in the municipality of Geta, in the northern parts of the Åland islands (Fig. 6). The study area consists of well-exposed and polished rapakivi granite outcrops displaying a NE-SW trending dextral strike slip fault with a minor reverse component of slip and a well-developed damage zone.

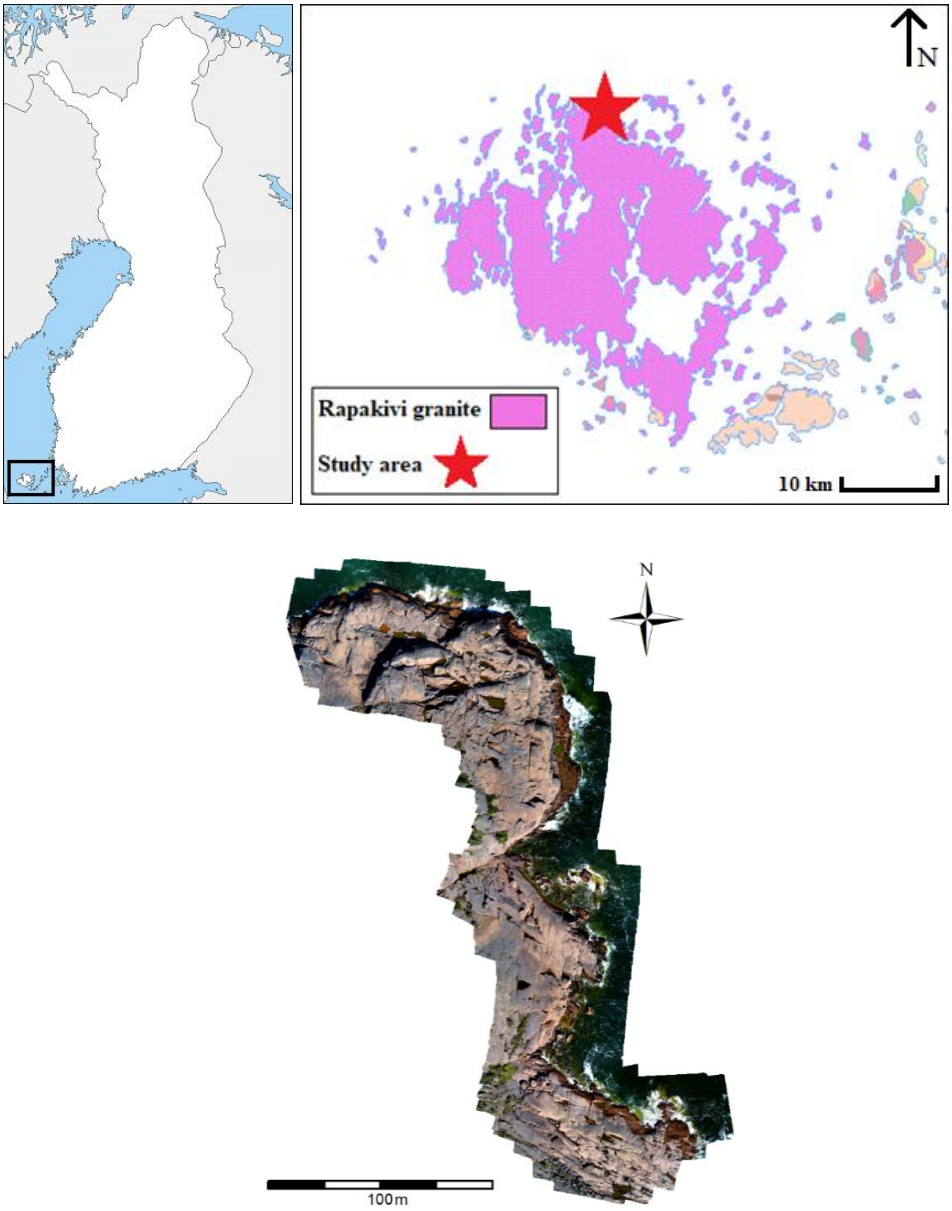

Figure 6: Overview of the study area location of the Geta fault attached with orthophotomosaic image produced by UAV at a flight elevation 20 m, with pixel size of 0.55 cm.

2.3 WORKFLOW

2.3.1 Field observations

Detailed field observations of the Geta fault were made to get an overview of the fault and the fracture network characteristics within its well-developed damage zone. The main goal was to characterize in detail the fault geometry and the different parts of the

associated damage zone. In addition, the work aimed to further complement the geological interpretations of the drone-based 2D and 3D aerial photogrammetry as well as to provide the guidelines for sampling. Since small details e.g., fracture fillings, fracture kinematics and relatively short fractures are roughly impossible to determine from aerial photogrammetric material, the field observations were necessary. Although the drone-based data were comprehensive, the study site topography caused errors in photogrammetry thus detailed study and manually taken measurements were required to get more reliable results.

During field observations the Geta fault was divided into different segments according to its varying geometry to make the field sketching more representative and convenient and to help making clear interpretation overview of the fault, its different characteristics and their linkage to each another. The measured parameters were dip and dip direction of fault slip surface, fracture orientations of different parts of the damage zones, dip and dip direction of slickenside surfaces and associated striations. The striations (slip lineation) were measured using the pitch method and further calculated to the standard trend and plunge format with Orient. A total of 67 tectonic measurement were taken and used in further structural analysis in stereographic projections to support the digital mapping made on CloudCompare (Section 2.4.2). Observations were measured with Freiberg geological compass, hand-written manually to notebook and further digitized and plotted on GeOrient. Other measured parameters were fault core width and fault trace length. Since the study area is located at homogenous isotropic Åland Rapakivi Batholith, the lithological variations were little to non-existent. Principally the only rock type observations were of fault core features; core alteration and cataclastic veins and possible fracture fillings.

Fieldwork included:

i. Characterizing fault geometry: slip surface, extensional and contractional steps (bends), linking step-over, fault splay towards possible NE termination and length & width of the fault.

ii. Slickensides and striations within the fault slip surface.

iii. Characterizing different damage zones and their structural features; geometry, S-C structures, striations and relation to the main fault geometry.

iv. Footwall and hanging-wall fracture observations (fault vicinity)

v. More detailed characterization of the fault core (e.g. fracture intensity, veins, kinematics etc.)

vi. Mapping of smaller fault on the E-side of the main fault.

vii. Sampling and photography

2.3.2 2D-fracture network mapping

A regional 2D fracture network mapping around the Geta fault was done based on aerial photogrammetry that were produced by UAV at a flight elevation 20 m, with pixel size of 0.55 cm. Drone images were taken with a minimum of 60-70 % overlap and georeferenced using VRS-GPS ground control points. Further, the images were processed into orthomosaics by using Agisoft PhotoScan software (Agisoft, 2018), done by Nicklas Nordbäck, GTK.

The idea was to generate trace-map with faults and dominant trends of regional fracturing around the Geta fault with support of stereographic projections based on measurements taken at the field, in order to evaluate the relationship between fault-induced secondary and regional fracturing (e.g. how does the fault and syn-fault fractures control the regional fracturing of the area). Further, this data will be used as a reference material in comparison to 2D-fracture network data produced in KARIKKO-project. In addition, with the help of Turku PET-center, artificial intelligence assisted image pattern recognition may be used in grinding tomography data processing the topology of fracture networks.

Fracture digitization was made on ArcGIS by manually drawing polylines on top of the fracture traces seen on drone-acquired ortophotos. In order to create reliable topology, fracture trace digitization had to be done with snapping option on, otherwise certain unconnected traces would appear as errors in topology analyses (Nyberg et al., 2018). Once the fracture traces were extracted, topology properties were analyzed by using Fractopo analysis tool by Ovaskainen (2020). The digitized traces were first validated

within the Fractopo to sort out problematic traces e.g., V-nodes, multijunction and overlapping nodes, and later analyzed for various parameters.

2.4 DIGITAL OUTCROP MODEL

2.4.1 Photogrammetry applications in structural geology

The principle of photogrammetry is triangulation which is based on capturing a minimum of two two-dimensional photographs from different viewpoints and further "lines of sight" can be obtained from camera to points on the target. Afterwards, the lines are intersected mathematically in order to produce three-dimensional coordinates from the target points.

Digital photogrammetry (=DP) is a fast advancing survey technology for structural geology. In DP 3D model is obtained by using SfM (=structure-from-motion) method, which can be utilized with several different methods, for example, an unmanned Aerial Vehicles (UAVs). With a help of UAVs, photogrammetry technology allows capturing high-resolution three-dimensional geological data from study sites by fast, safe and inexpensive ways. Large digital datasets can be obtained in short periods of time, resulting in more representative and accurate results of study site features, without problems that are encountered in traditional mapping methods, such as safe accessibility (e.g., Eisenbeib, 2009; Carrivick et al., 2016). These datasets can further be used in digital structural analysis of planar structures (Riquelme et al., 2014; Vollgger et al., 2016).

2.4.2 CloudCompare

Photogrammetry datasets can be imported to CloudCompare (Girardeau-Montaut, 2015) which is an open source 3D visualization and computation software. Software is specifically designed for processing 3D point clouds but use of triangular meshes is also applicable (Thiele et al., 2017). Software includes two structural geology plugins: Compass by Thiele et al. (2017) and Facets by Dewez et al. (2016) which both can be used to extract data from 3D point cloud by manual (Compass) and semi-automatic (FACETS) methods.

2.5 3D DOM OF THE GETA FAULT

A medium accuracy 3D point cloud model was generated from the Geta fault area by Nicklas Nordbäck, GTK. Overall, 1016 images were obtained from 1013 different camera stations at a flight elevation of 12.3 m with ground resolution of 3.07 mm/pixel at a

coverage area of 0.0117 km^2 per image. Data processing resulted in a 3D point cloud with a total of 78 217 287 points (Fig. 7). Data was processed with Agisoft Metashape Professional software, by applying the workflow represented by James (2017).

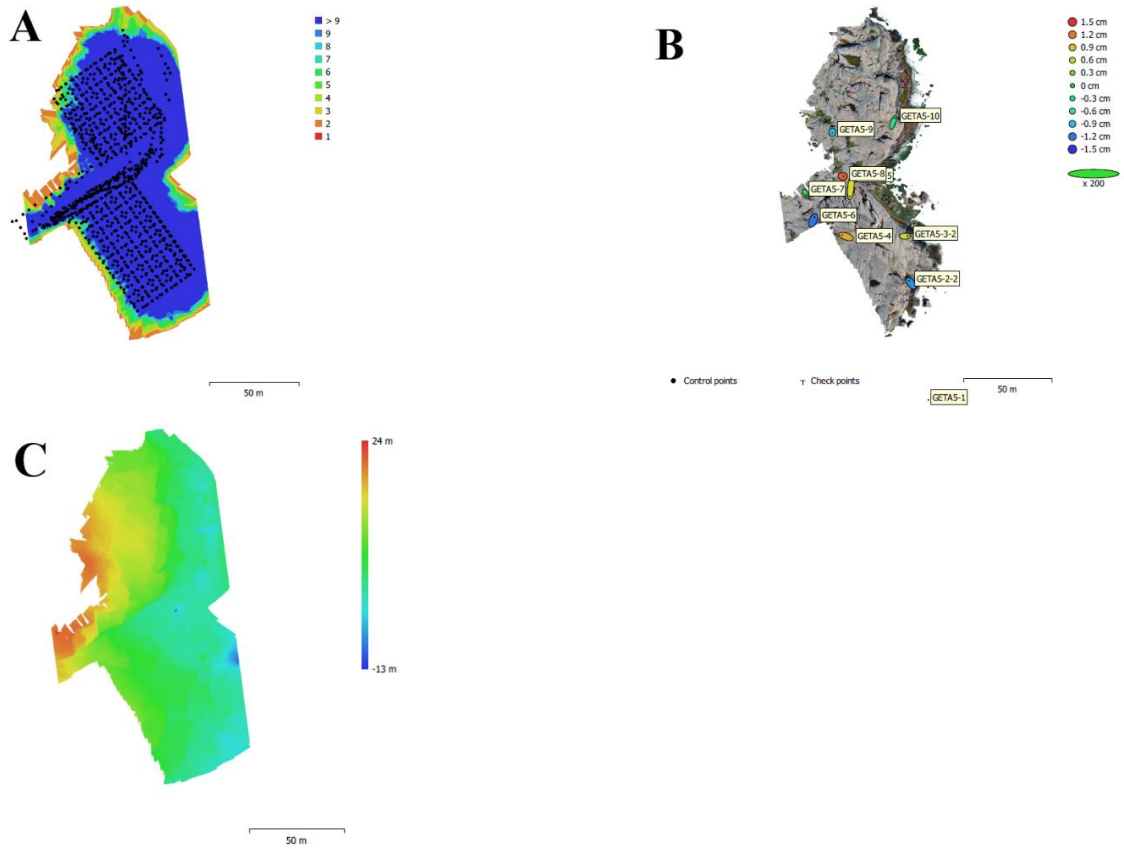

Figure 7: A Camera locations and image overlap. B GCP locations and error estimated. Z error is represented by ellipse color. X, Y errors are represented by ellipse shape. Estimated GCP locations are marked with a dot or crossing. C Reconstructed digital elevation model, with resolution 1.23 cm/pix and point density 0.662 points/cm^2

2.5.1.1 *Digital mapping and structural analysis*

DOM of the Geta fault was generated for purposes of further structural analysis of the Geta fault and fractures of the area by using CloudCompare open-source software (Girardeau-Montaut, 2015). The structures were mapped both manually, and semi-automatically using the Compass (Thiele et al., 2017) and Facet plugins (Dewez et al., 2016). The compass plugin was used for detailed mapping of the orientations of well-exposed fracture surfaces by applying the *plane* and *trace* -tool of the plugin. The *Facet* Kd-tree tool was used for extracting bulk planar data from the 3-D model and further, applied to stereogram tool for creating stereographic projection of all planar data derived from the *Kd-tree* tool.

2.5.1.2 *Facets plugin*

The Facets plugin allows automatically extracting planar facets from point clouds and further, the extracted data can be classified according to the orientation of the structures, for example, fracture planes (Dewez et al., 2016). Facets plugin has three different working aspects. 1. Data processing aspect implements with two different algorithms, each with minimum number of parameters, to divide the initial space into planar portions; using either a tree with k dimensions (k-d tree) or a fast-marching method. 2. Stereogram rendering tool to produce structural geology analysis with possibility to classify extracted data. 3. Possibility to export extracted data to third party software (3D GIS shapefiles or ASCII export) for further specialized interpretation (Dewez et al., 2016).

2.5.1.3 *Compass plugin*

The Compass plugin is designed especially for structural geology. The plugin allows measuring manually orientations, spacings and thicknesses. The orientation measurement computing is based on the standard plane-fitting techniques (Thiele et al., 2017). The plane tool is used to measure orientations of planar structures i.e. fault and fracture surfaces. Measuring orientations with plane tool from DOM works according to the least squares algorithm, where the measured plane is fitted to all points inside the 'measuring circle', resulting in an orientation estimate (Thiele et al., 2017). Trace tool allows the estimation of the structural orientation based on its intersection with varied surfaces. The trace tool uses least-cost path algorithm in order to track user defined start and end points by following intersection traces along the surface (Fig. 8) (Thiele et al., 2017).

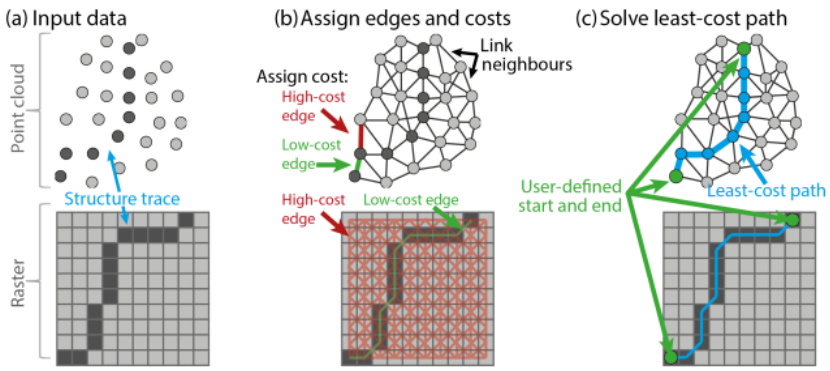

Figure 8: Illustrative pictures of the least-cost-path algorithm. Figure after Thiele et al. (2017).

2.6 SAMPLING & SAMPLE PREPARATION

Six different samples were taken from the vicinity of the Geta fault slip plane by using a hammer and a wedge. Sampling sites were chosen based on field observations, each

sample representing different types of damage zones (Table 1). All of the samples are Rapakivi granites, comprising of relatively fine-grained groundmass and larger, porphyric grains of feldspar, quartz and biotite. Color variations across the samples are minor, and the variations were mainly due to the quantity of biotite grains. Samples had no visible microstructures either fabrics to the naked eye. On each sample, a North arrow and horizontal lines to preserve information of the original orientation of the sample.

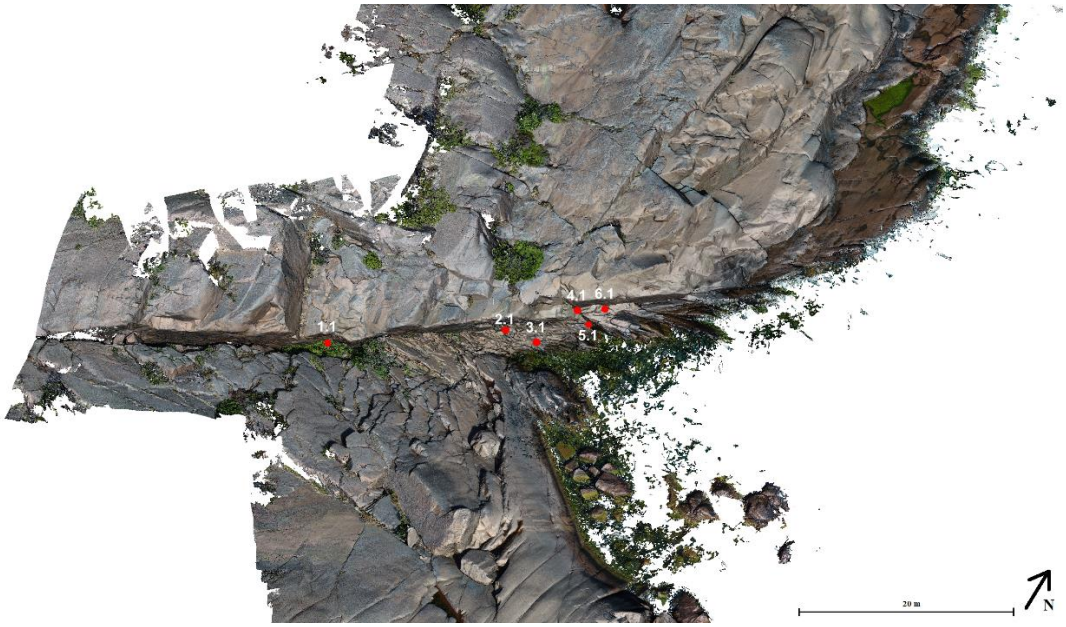

Figure 9: Sample sites marked on a screenshot from CloudCompare.

Table 1. Sample IDs.

Sample ID	DZ type, types of observed fractures at sampling location
1.1	Fault bend DZ (releasing) + fracture networks
2.1	Tip/wall DZ + wing-cracks
3.1	Tip/wall DZ + wing-cracks
4.1	Fault-step, linking DZ + mode I tension fracture zone
5.1	Fault-step, linking DZ + main slip surface zone
6.1	Clastic dyke, shooting off from the fault core

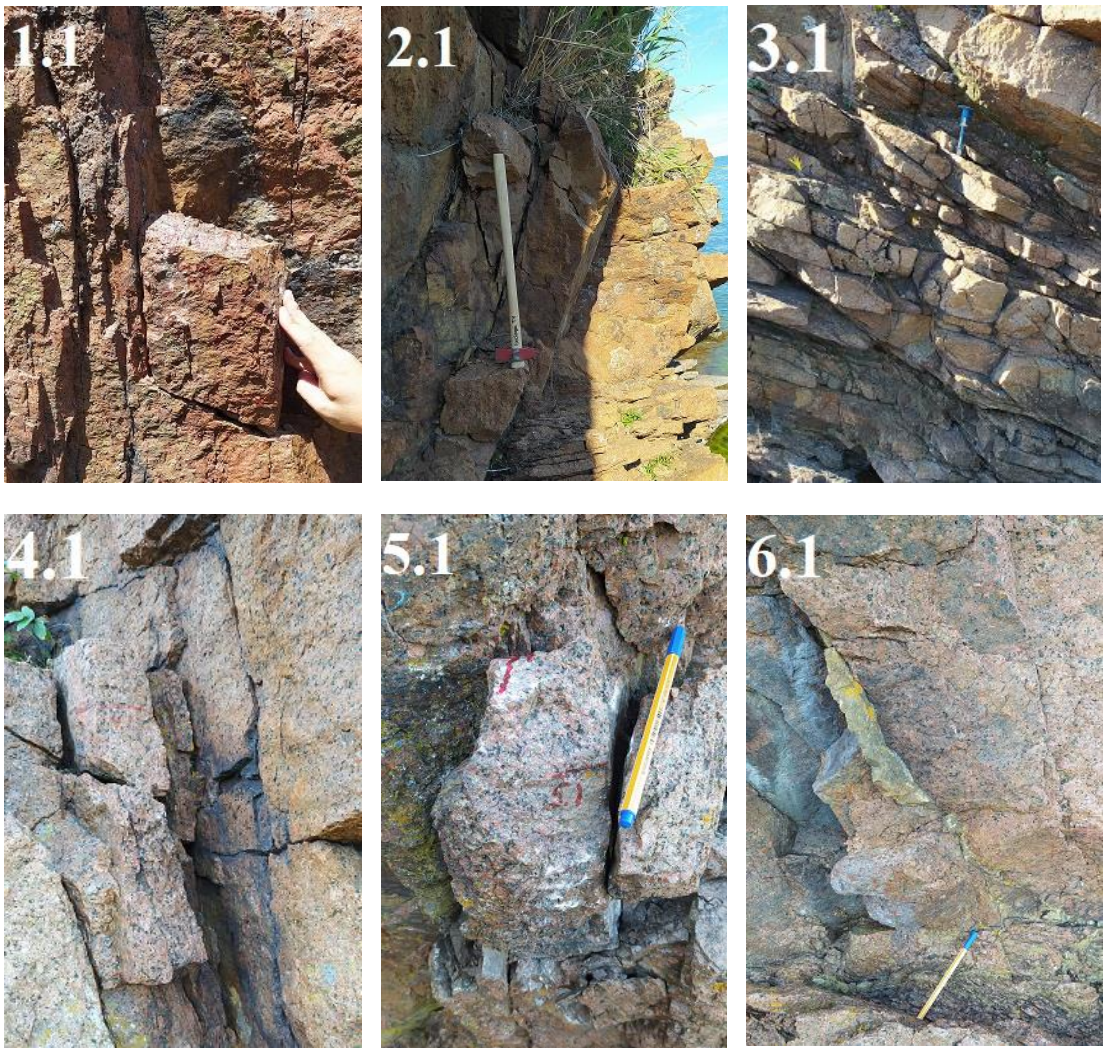

Figure 10. Geta fault sampling sites with field characteristics of the fault and fault-induced secondary fracturing. Sample 1.1: Releasing bend (extensional) damage zone. The sample is bordered by N-S trending vertical fractures. Sample 2.1: Between main slip surfaces, close to intensely deformed fault core. Sample 3.1: Damage zone networks accommodated by wing-crack fracturing with semi-steep fractures in wing-crack bound sheet. Sample 4.1: Mode I tension fracture zone hosted by fault-step with contractional restraining bend characteristics. Sample 5.1: Linking damage zone, associated by typical intense linking damage zone fracturing occurring at fault-step at the immediate vicinity of main slip zone. Sample 6.1: NW-SW orienting sub-vertical clastic dyke shooting of from main fault core.

All samples except 6.1 were cut with rock saw and then drilled with Shibuya TS-092 core driller into 50x50/60 mm sized drill cores, in order to fit them perfectly into GRN16 3D-grinder. Few of the samples were difficult to drill due to their small size and considering that the original orientations had to be maintained. In addition, some of the cores fell apart while drilling since they were intensely fractured.

2.7 AUTOMATIZED 3D-GRINDING TOMOGRAPHY

The method was also applied to the grinding tomography data, as in the purpose of producing the third scale of the study (comparisons at different scales), as well as observing at how topology-ratios change within same sample when slices are analyzed of

different depths. The tomography images were georeferenced with QGIS to their original sampling locations so that their orientations and actual geometric sizes correspond to reality.

2.7.1 Application of tomography methods in geosciences

Tomography methods are generally used for providing information inside the specimens by revealing cross-sections which can be visualized in 3-dimension and used to measure volumes and dimensions of internal features (Pascual-Cebrian et al., 2013). Tomography methods have been widely utilized in the field of geosciences, especially the CT-scanning, ever since it was introduced in 1973 (Hounsfield, 1973). It has been used for example, in study of paleontology (Conroy and Vannier, 1984), petroleum geology (Wellington and Vinegar, 1987; Withjack, 1988) fluid-flow (Anderson et al., 1992) and porphyroblasts and mineralizations (Sayab et al., 2015). Faulting has been studied by CT-scanning through scaled models by Schreurs and Hänni (1998), in addition to fracture propagation in rock samples by Nasseri et al. (2011). Grinding tomography methods have been previously used to study the structure of fossils (Pascual-Cebrian et al., 2013).

Tomography methods can be divided into two categories: non-preservative and preservative tomography methods. In preservative methods, the sample is preserved in experiment by using e.g., X-ray (CT, XMT or SRXMT), neutron-tomography or MRI instrumentation, whereas the non-preservative methods are done using grinding equipment or similar, eventually destroying the sample during the experiment (Pascual-Cebrian et al., 2013). X-ray tomography (=CT-scanning) measures the attenuation coefficient of the material and is based on capturing a series of 2D planar X-ray images and reconstruct the data into 2D cross-sectional slices. This technique provides volumetric information and the density properties can be displayed as 3-dimensional voxel X-ray attenuation maps, thus revealing the internal features of the material (Pascual-Cebrian et al., 2013). The images can show for example fracture patterns, quantification of mineralogies and porosity (Wellington and Vinegar, 1987) and reveal spatial distribution, shape and geometry of matrix foliation of porphyroblasts as well as millimeter-scale compositional layering of mineralizations (Sayab et al., 2015).

In non-preservative tomography methods such as grinding tomography method, the sample is grinded using manual or automatic grinding equipment exposing several surfaces of the sample. After each grinded layer, the data is captured by digital methods such as high-resolution camera or scanner (Pascual-Cebrian et al., 2013).

2.7.1.1 *Collection of grinding tomography data with GRN16-grinding machine*

In this Thesis, the goal is to reach whole new level of grinding tomography method by constructing accurate 3D-micro tomography models of fracture networks within rock samples from data captured with GRN16 grinding machine of University of Turku, and present new solutions for problems of grinding tomography methods (Appendix. 1) discussed by Pascual-Cebrian et al. (2013).

GNR16 grinding machine is initially developed for automatized grinding of thin section samples. The machine was ordered by University of Turku in 2016, after which it has been under active co-operative development together with various collaboration partners such as Astera Solutions Ltd, Apex automation Ltd and Winkoms Open Microscopy Ltd. Throughout this development, we have reach a point where the machine is equipped with attachments which allows automatized acquisition of 3D grinding tomography data.

GRN16 3D-grinder is a modified automatic grinding machine, equipped with Python-based 3D-software, which control the grinder and the attached camera system with visible light source and LED-UV-light source. Method utilizes automatized grinding tomography, providing the generation of 3D-tomography data from successive 2D-slices grinded and photographed at desired intervals (50 microns in this work).

Drill cores were sent to Geological survey of Finland for CT-scans for comparison data of two tomography methods. The data was further evaluated in two-dimensions i.e. what can be seen in CT-images and in grinding tomography images within the same samples and correlating height.

Drill cores were prepared for 3D-grinder, by first gluing them on 52*51 mm sized glass epoxy sheets used in GNR16 machine. Gluing was done by mixing a two-component adhesive. Prior to the gluing, sample ID and North arrow were carved in the middle of the glass sheets, avoiding the glass margins as it may cause leakages in the vacuum of the machine. As the glasses were ready for gluing, a few drops of glue were dripped over them, after which the sample was pressed on to the glass. Sliding and moving the sample carefully on top of the glass sheet ensured that no air bubbles remain between the sample and the glass sheet. When the air bubbles were removed and the sample point in the desired direction, it was placed to dry on a thermal plate at 50° C temperature overnight. After gluing, the samples were ready for the grinding process, which was started by “leveling grinding” to ensure that the sample surface was perfectly even, and then the

actual grinding could be started. Due to the extreme long grinding process, only three samples were chosen for this study (Geta-1.1A-20, Geta-1.2-20 and Geta-4.1-20). Sample Geta-1.1A-20 was also impregnated with fluorescent epoxy to test the UV imaging in addition to normal imaging.

2.7.1.2 *GNR16 grinder workflow*

The first step of the process is to fix the diamond wheel in place and use towel to protect the sample table. Afterwards the sample table is cleaned carefully in order to reach vacuum, for holding the samples intact. The vacuum is reached by blocking the vacuum holes either with glasses or specifically manufactured stainless steel rim which can fit up to four 50*50 mm glasses. When the vacuum is at acceptable level (>90 units on the display), the machine is adjusted to the desired settings (Table 2) and is ready to start. With the vacuum and steel rim holding the samples in places, the sample table rotates so that the diamond wheel grinds off slice of a defined thickness of the sample, in successive steps until a desired thickness is reached. After each grinding step, the machine dries the sample surface from lubricant water with pressurized air and takes a photograph of the sample surface in both visible and UV light, and registers the Z-coordinate of the sample surface into the image file, in addition the X- and Y -coordinates are also stored automatically. After photographing, the grinding process continues as long as the predefined final grinding depth is reached. The XY-position of the images from successive grinded steps (different Z-levels) can be further aligned by using Align-app, which correlates the recognized elements and patterns within the image files and adjusts the XY -position of each image. Subsequently, these adjusted images may be used to construct 3D-tomography models. For purposes of this Thesis, image sequences are used in studying fracture network systems; however, the possibilities of the use are unlimited as long as the interval shows visual contrasts, (normal or UV light).

Table 2. The most relevant parameters for the study.

Parameter	Value	Notes
Wheel type	140	Must be measured before setting in.
Feed rate	20-100 µm / min	Dependent on wheel condition and sample characteristics.
Table speed	30%	*Default*
Spindle speed	2000 rpm	*Default*
Grinding depth	50 µm	The depth each grinding cycle grinds. Can be set to desired thickness.
Liquid	Water	*Default*
Safe vertical	*x* µm	The height where the diamond wheel sets when starting the process.
Spindle torque: surface detection	0.12 Nm	Force applied on sample surface when detecting the samples at start of the process.
Grinding time: finishing	0 min	Set to zero in order to save time. Useless parameter for purposes of this study.
Target thickness	*x* µm	Can be set to desired thickness. Useful when the entire sample is close to finish.
Height of wheel	25900 µm	Must be measured before setting in the diamond wheel.

3 RESULTS

3.1 CHARACTERIZATION OF THE GETA FAULT

The Geta Fault is a NE-SW trending sub-vertical dextral strike-slip fault associated with sub-horizontal plunging striations, indicative of a minor reverse component of slip. Overall, 10 slip lineations were observed, characterized by sub-horizontal WSW-plunges. The fault comprises of footwall and hanging wall with separated by a steeply NNW-dipping slip surface. The fault core is altered and associated with well-defined, intense fracturing. The lateral extent of the exposed trace is about 80 meters with indications of splay-type fault termination at the NE parts (Figs. 12 and 13). Towards the South, fault core is mainly open and eroded with width approximately 20-40 cm, the “canyon” hosts obliquely eroded slickensides averaging orientation 109/90 with representative slip lineation averaging 019/71, which indicates that the W-block has moved upwards, indicating a minor reverse component of slip. Main fault width varies between approximately 1 meter to 20 centimeters and is mostly open and eroded. Fault core is well-exposed in two locations of the central parts of the fault, with 25 cm thick intensely deformed altered core zone (351/83 Fig. 11b), with a clastic dyke shooting of from main fault (Fig. 10 - 6.1). Fault slip surface at the exposed core zone average orientation is 316/71.

The Geta fault is characterized by well-developed secondary fracture patterns defining the different types of damage zones (Figs. 12 and 13; “I-V”). In the Southern parts, the main fault splits into branches and is only partially exposed due to increased vegetation, however, gently NE-dipping DZ-fracturing were observed with overall three measurements taken (042/28, 033/31, 040/32). Southern-central parts, where the fault trace is still properly exposed, steep fractures extend as planar surface 2 to 5 meters and some even larger. The damage zone fracturing displays distinct patterns that are associated with the dextral sense of movement along the fault. Fractures occurring in the different types of damage zones display variation in dip directions and dips, whereas the fault slip surface attitude remains fairly constant, except in the fault bend DZ (releasing and contractional) and in the linking DZ (contractional step Fig. 13; “I-III”). Particularly characteristic is the footwall, which hosts wing-crack type damage zone fracturing with mostly gentle dips towards NE-NNE. The most distinctive damage zones are wall/tip combined of linking (contractional step) and fault bend (extensional releasing bend and

contractional step) types. Further, indications of approaching damage zone are present towards linking DZ in SE, where the main fault interacts with a smaller strike-slip fault. Fault HW-side show less distinct damage zone fracturing, although the damage zone extends approximately 7 meters, with fracture orientations averaging 077/00. Regional fracturing on the hanging wall side > 10 meters away from the fault appears mainly random, with low fracture intensity and no distinct sets.

Fault bend DZ (extensional and contractional) **(I-II):** The main slip surface at the central section is curved and shows extensional releasing bend characteristics and is immediately followed by contractional step on the SW side of the bend ("I-II"; Fig. 13). The fault bend damage zone, both extensional and contractional parts are characterized by sub-vertical NWN-SEE oriented fractures with relatively steep dips, thus the extensional part display also sub-fault-parallel fracturing (WSW-ENE) also in the vicinity of inferred damage zone, secondary fractures are dipping more gently towards SE ("I-II"). Close to the releasing bend, HW-fracturing has more gentle dips, whereas in overall, fractures within hanging-wall are steeply dipping east in the immediate vicinity of the fault.

Linking DZ (contractional step) **(III):** Restraining contractional fault-step at the central parts is featured zone with intense mode I tension fracture zone, with indications of steeply dipping intense linking damage zone fracturing (278/77 "III"; Fig. 13). In the immediate vicinity of slip surface, linking damage zone is associated with chaotic fracture trend, dipping in SE, while faults footwall tip/wall DZ sections are characterized by NE-NNE dipping wing cracks ("III-V"; Fig. 13). However, linking DZ fracture orientations are gradually "normalizing" towards fault splay termination in NE.

Wall/tip DZ **(IV):** The wall DZ next to the fault bend is characterized by very intense fracturing with two main orientations displaying more gentler dips than in bend damage zone ("IV"; Fig. 13). Wing-cracks splaying from the central sections of the fault have the same orientation with those splaying from the possible NE termination, this may indicate either former tip points or sticking points ("IV").

Wall/tip DZ **(V):** Towards to fault termination, the wall/tip damage zone display again very intense wing-crack type fracturing on footwall side, occurring sub-oblique to and abutting against the fault. The fracture dips gradually change more gentler towards to the fault termination in NE ("V"; Fig 13.) Wall/tip DZ featured by constant strikes with

variation in fracture dips, which reveals S-C type structures, as the thicker wing-crack bound sheets are associated with systematic steeper fractures that are compatible with a SW-block-down shear sense within the DZ (Fig. 11c.). The Northern part is also hosting slickensided R-planes with average orientation (334/67) together with sub-horizontal slickenline averaging (07/SW).

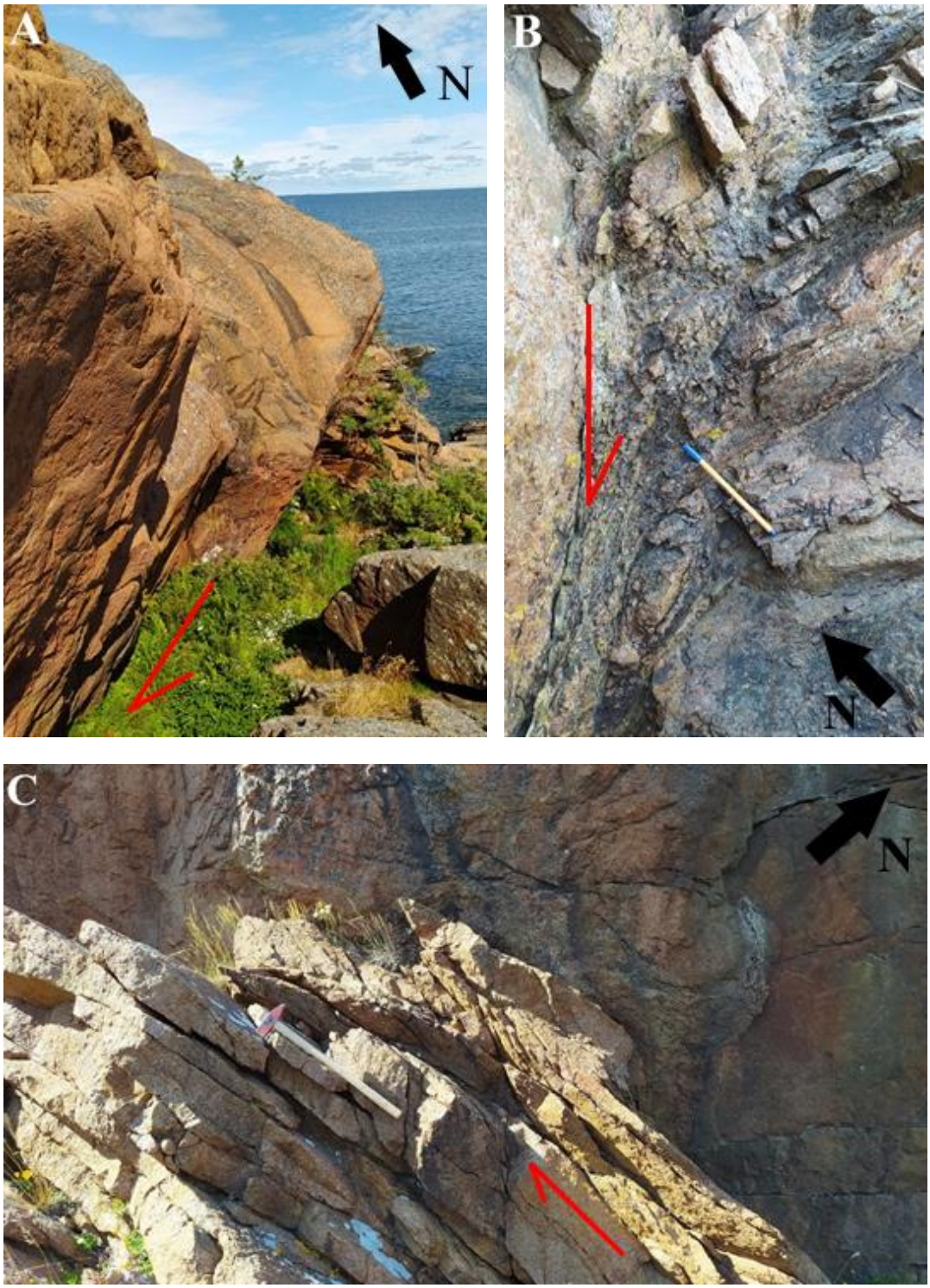

Figure 11: Field characteristics of Geta fault and its damage zone. A: Releasing bends along the central part of the Geta fault. View towards NE. B: Intense fracturing between main slip surfaces defining an altered core zone (351/83) (bottom part of the figure) and well-developed wing-cracks. Pencil for scale,

blue head pointing towards North. C: Systematic steep fracturing (019/69) in wing-crack bound sheet (052/39), compatible with SW-block-down shear sense within the tip/wall DZ.

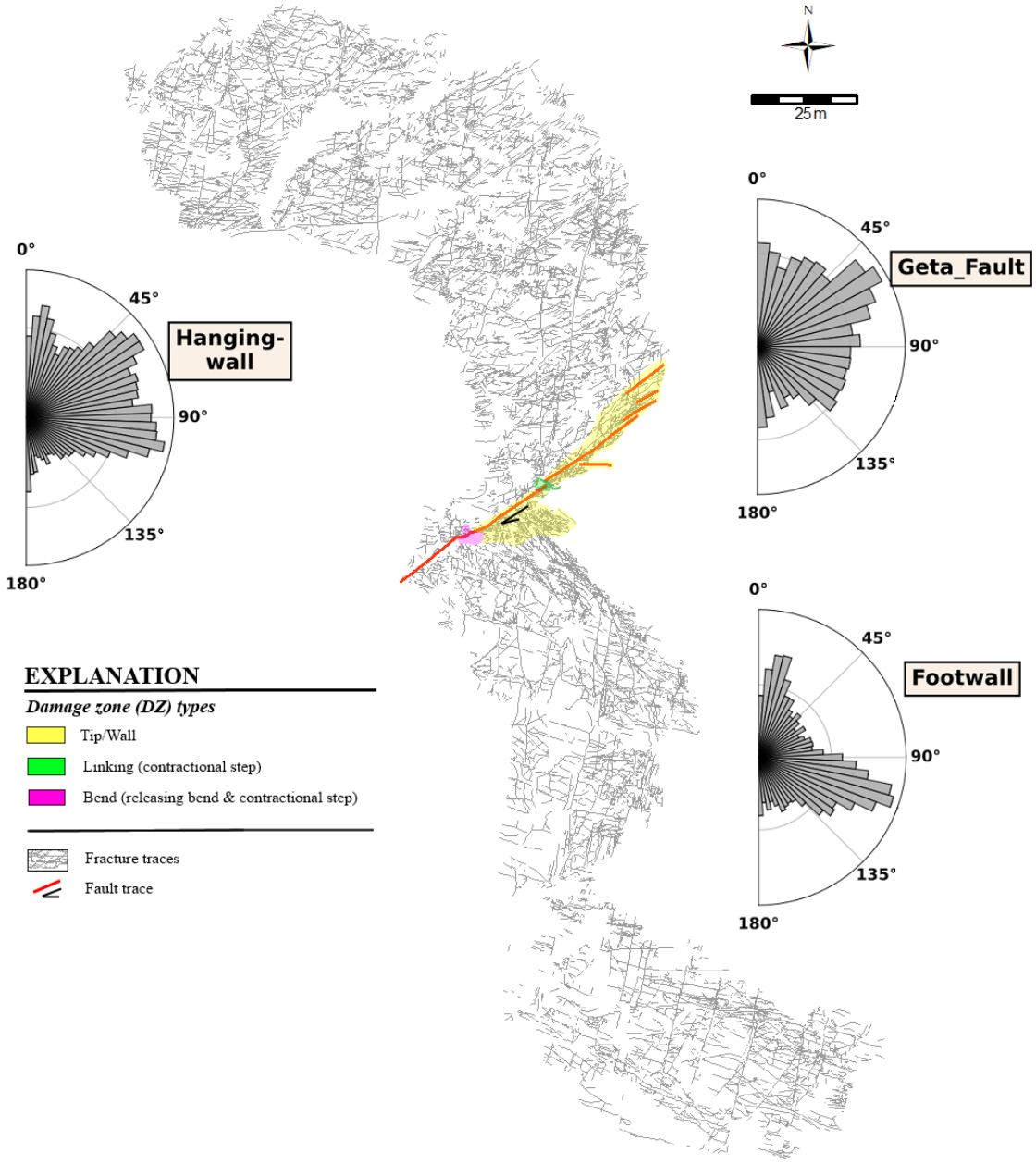

Figure 12. 2D overview map of the Geta fault and surrounding outcrops with the recognized fault and associated different types of damage zones. Roseplots from fractopo analysis highlighting the dominant fracture trends on different parts of the region, where Geta fault acts as a dividing feature. Hanging-wall is located in the NW side of the fault trace and footwall is in the SE side of the trace.

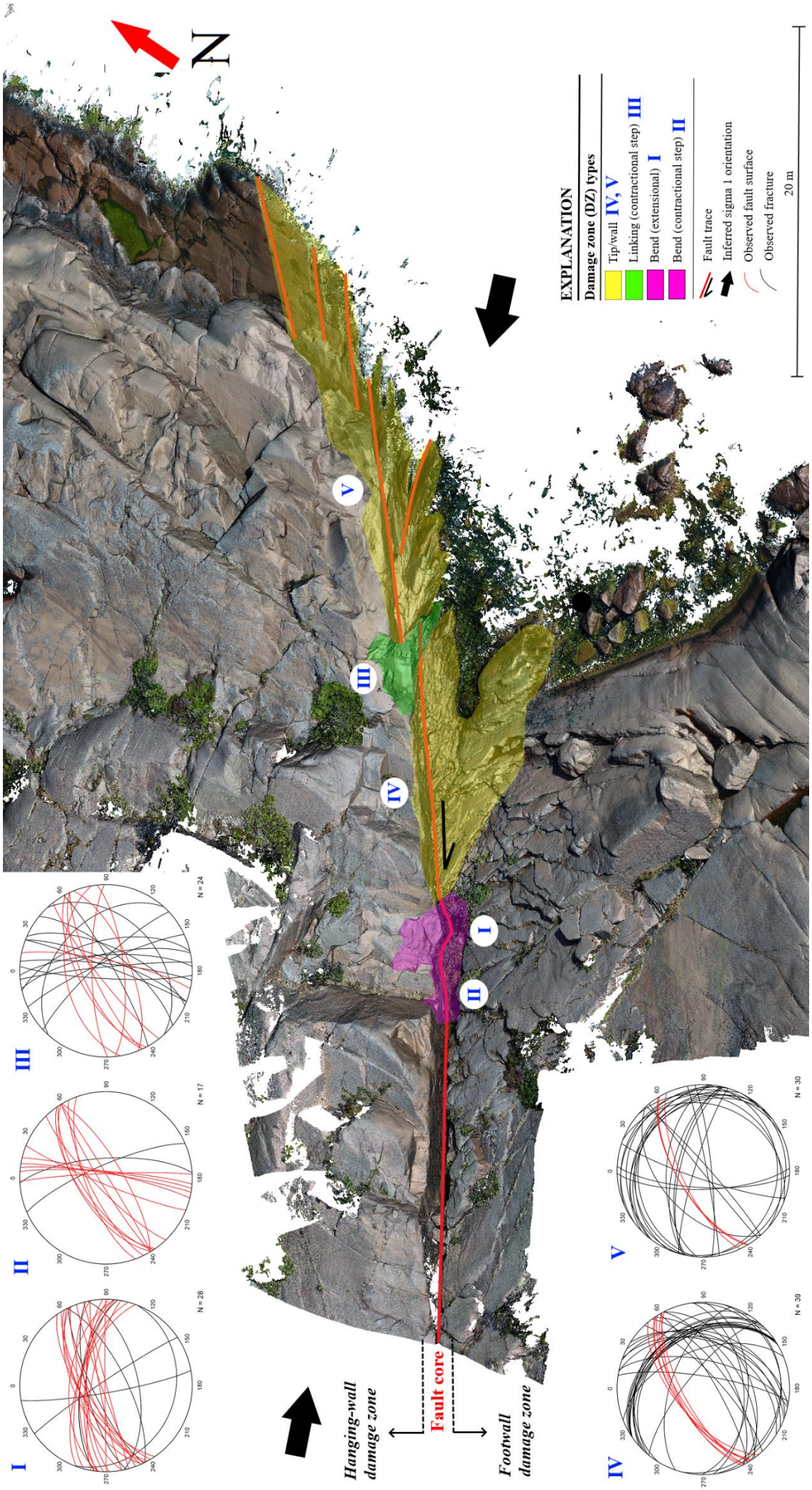
N
EXPLANATION
Damage zone (DZ) types
Tip/wall IV, V
Linking (contractional step) III
Bend (extensional) I
Bend (contractional step) II
Fault trace
Inferred sigma 1 orientation
Observed fault surface
Observed fracture
20 m
V
III
IV
I
II
Hanging-wall damage zone
Fault core
Footwall damage zone
I
N = 28
II
N = 17
III
N = 24
IV
N = 39
V
N = 30

Figure 13. More detailed 3D-map overview of the recognized distinct damage zones. The lower hemisphere stereograms show measured orientations of the fault slip surfaces and the fault-induced secondary fracturing within different types of damage zones. The measurements are a combination of field observations and virtual 3D-mapping on CloudCompare.

3.2 STRUCTURAL INTERPRETATION BETWEEN FAULT-INDUCED AND REGIONAL FRACTURING

Fracturing across the study area can be divided into three main orientation sets based on the spatial variations of the fracture orientations. The area is characterized by N-S to NNE-SSW (Set 1) trending fractures that are continuous across the whole study area, occurring almost unaffected by the Geta fault. The NE-SW (Set 2) trending fractures are present in the fault vicinity and within the hanging-wall (Fig. 12). Fault hanging-wall side (W) is mostly characterized by the sub-fault parallel Set 2 fractures, yet it is associated by most variable fracture patterns. The footwall side (E) is particularly characterized by the WNW-ESE (Set 3) trending fracture orientations. However, in the most northern parts of the study area the dominant fracture trend is WNW-ESE trending Set 3.

Set 1 (N-S to NNE-SSW) fractures are relatively long and continuous across the study area and are cross-cut and abutted by Set 2 (NE-SW) trending fault parallel fractures and by Set 3 WNW-ESE trending fractures. The orientations are seemingly dependent on which side of the fault they are associated spatially, as the Geta fault acts as a dividing feature in the region. The fracture intensity occurs fairly constant around the area, with a few exceptions at e.g. fault damage zone on footwall side, where the fracture patterns are also relatively complex in the vicinity of the fault. When it comes to assessing the connectivity of the area, different topology parameters show very little variations between the divided spatial domains and the results plot seemingly similarly in every domain (Fig. 14; XYI and branch ternary plot). The most dominant node type of the area seems to be isolated I nodes with comparatively few Y and X nodes (Fig. 14; XYI).

Based on the cross-cutting and abutting relationships between the fracture sets, the regional long Set 1 (N-S to NNE-SSW) trending fractures could be the oldest and therefore pre-date the formation of Geta fault and therefore, also the syn-fault generated Set 3 (WNW-ESE) oriented damage zone fracturing and Set 2 (NE-SW) fault-parallel fracturing. However, as the whole footwall side is characterized by WNW-ESE dominant fracture trend, it is impossible to infer, how far the damage zone extends. However, another smaller fault strike-slip fault is associated in the Southern part of the footwall side, characterized by the same dextral sense of movement, and may be the reason for the large far extent of the WNW-ESE oriented fracture Set 3. The hanging-wall side shows

more variation in fracture trends but is mainly characterized by aforementioned Set 2 fracture trend, which mostly terminate to Set 1 (N-S) trending fractures.

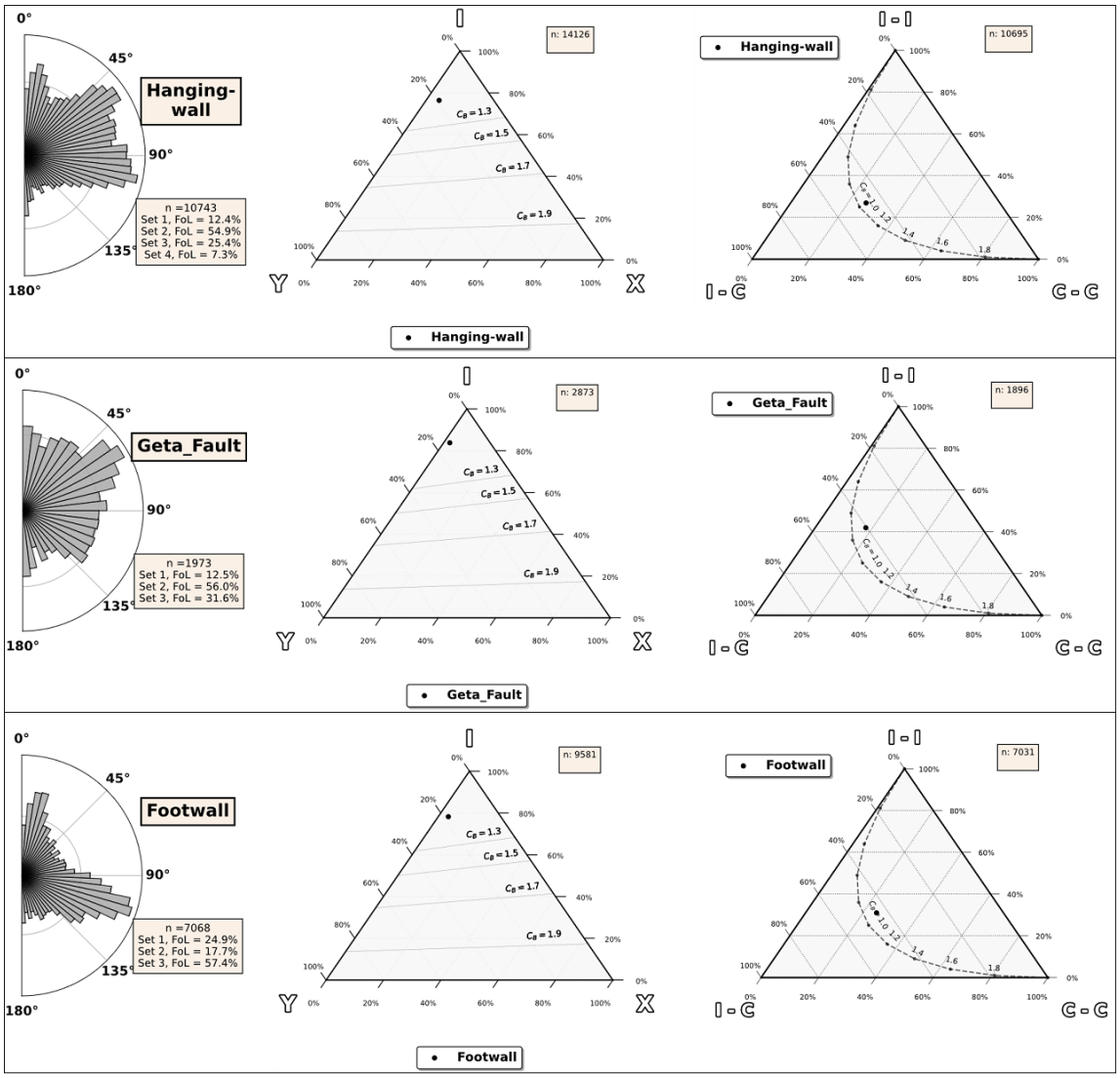

Figure 14: Rosette plots with attached XYI and branch ternary plots of the Geta fault, which were sub-divided into; Hanging-wall, Fault and Footwall domains.

3.3 GRINDING TOMOGRAPHY

A total of 1270 slices were grinded at 50 µm intervals and imaged from three individual samples, where recognizable features are different kind of fractures e.g. quartz veins, healed fractures with altered mineral infills, joints observed with fracture initiation and propagation patterns and intracrystalline fractures. Out of three samples, two were associated with close to same number of fractures (1.1A and 2.1), whereas third sample (4.1) had very few fractures. Overall, the amount of fractures was much smaller than expected in all samples.

The grinding data allows observing the microstructures in fine detail as the images have high-resolution. Alteration of small healed fractures is observed across each sample. Alteration occurs mainly through the healed fractures, as the altered fracture infills have spread along the lines of mineral lamellae (feldspars) and through intercrystalline fractures in quartz grains or in the edges of quartz vein, also the biotite grains are generally partially altered. Fractures bearing altered infills inside the mineral grains were generally smaller than the fractures which were continuous across the sample. Fracture orientations across the samples is overall compatible to macroscale fault-induced secondary fracturing along the damage zones.

3.3.1 GETA-1.1A-2020

Sample Geta-1.1A had the largest thickness of all the samples, with a total of 35 754 microns (51 835 - 16 081) and resulted in 560 images of which 538 were successful. The sample is from fault bend damage zone which has extensional releasing bend characteristics. The sample is characterized by mainly isolated short-length WNW-ESE trending healed cracks (Fig. 15; “II”) with altered mineral infills. Certain joints have signs of fluorescent epoxy, which means that sample have had pathways for epoxy to be absorbed, even there are no open joints visible to the naked eye. The sample is associated with a few NW-SE fractures that cross-cut WNW-ESE trending fractures at angle of approximately of 45° (Figs. 17a and 15; “I”) compatible with similar cross-cutting fracture pattern than in sample 2.1 (Fig. 17c and 16; “I”). However, no clear continuous fracture patterns are observable, as they are visible for only a few slices when moved deeper in tomography. Feldspars, quartz and biotite grains are associated with greenish colored alteration across the sample (Fig. 17d). In feldspars the alteration occurs particular in feldspar weakness (lamellae) directions (Fig. 17b), whereas the alteration within quartz grains is associated through intercrystalline fracturing. In biotites the alteration has progressed in the most extensive ways, as it has spread across several minerals, with no visible intercrystalline pathways observed for altering fluids/infills.

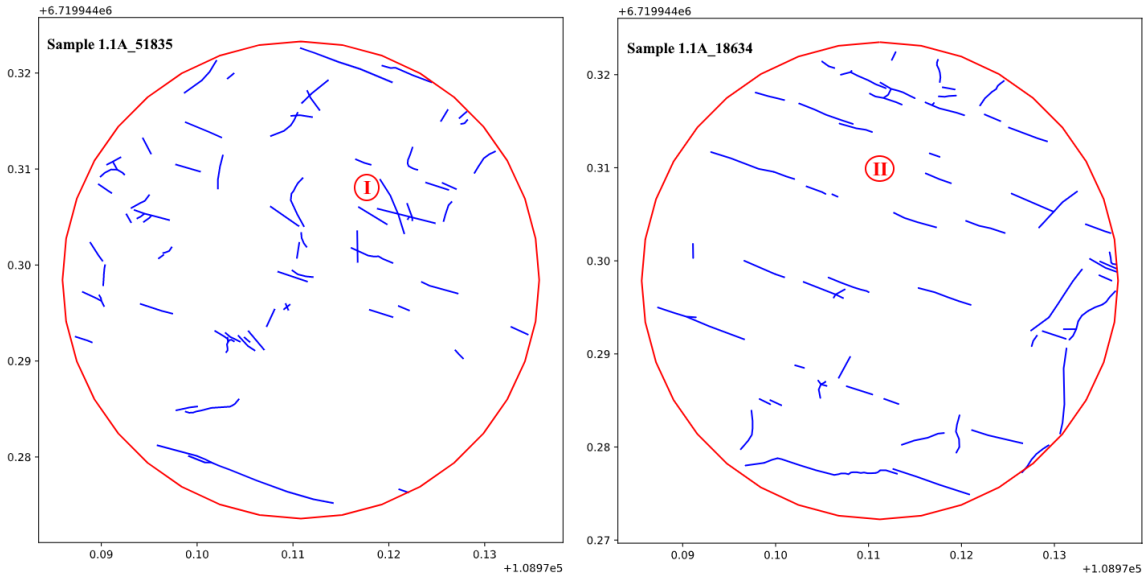

Figure 15: Base visualization of fracture traces in sample 1.1A.

3.3.2 GETA-2.1-2020

A total thickness of 23 582 microns (38 711 - 15 129) was grinded and imaged from sample Geta 2.1, taken from between fault slip surfaces, resulting in 355 images. Two of the images were disturbed and therefore total of overall 353 images were successfully aligned to x, y and z -coordinates. The dominant fracture patterns associated with sample 2.1 are E-W oriented fractures with gently curved traces and NW-SE trending secondary fracture that first abut and then crosscut the E-W trending fracture at an angle of 45° (Figs. 16; "I", 22, 23), striking in clockwise from the E-W fracture, compatible with dextral sense of movement. The E-W trending fractures are continuous across the sample and are approached by the second NW-SE trending secondary fracture, which occurs as approaching fracture in the same orientation as the first secondary fracture with corresponding direction and angle relation to the E-W fracture, without abutting or crosscutting it at any observed slice (Figs. 16; "II", 22 and 23.) Sample is also characterized by relatively thick NE-SW oriented quartz vein (Fig. 17e). Alteration occurs similar as in sample 1.1A (Section 3.3.1).

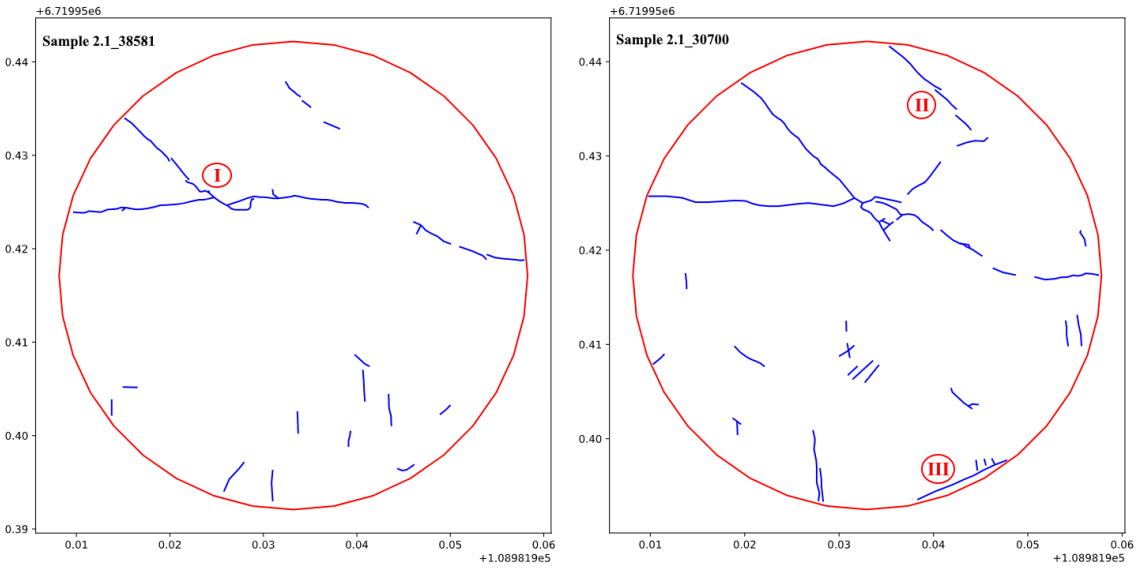

Figure 16: Base visualization of fracture traces in sample 2.1.

3.3.3 GETA-4.1-2020

Sample Geta-4.1 was grinded together with sample 2.1 (thickness of 23 582 microns (38 711 - 15 129), resulting in a total of 355 images, however, the sample 4.1 had relatively many disturbed images due to problems related to the grinding process (Appendix. 1). Even after image alignment, images of the sample 4.1 were mostly directed inaccurately relative to each other. Some features could still be observed. The most distinctive feature of the sample 4.1, taken from the contractional fault-step nearby the linking damage zone, characterized by mode I tension fracture zone, is the E-W trending isolated fracture which is continuous across the sample. The fracture trace is relatively straight with no signs of any curvature observed. At first, the main fracture has characteristics of a healed fracture with fracture fillings, gradually changing towards open fracture. Within the sample, smaller healed-cracks parallel to the main fracture, approach the main fracture trace. Sample also has less distinctive NE-SW fracturing oriented sub-parallel to the fault. The alteration is similar as within the previous samples. Due to the bad image quality no further analyses were made to this sample.

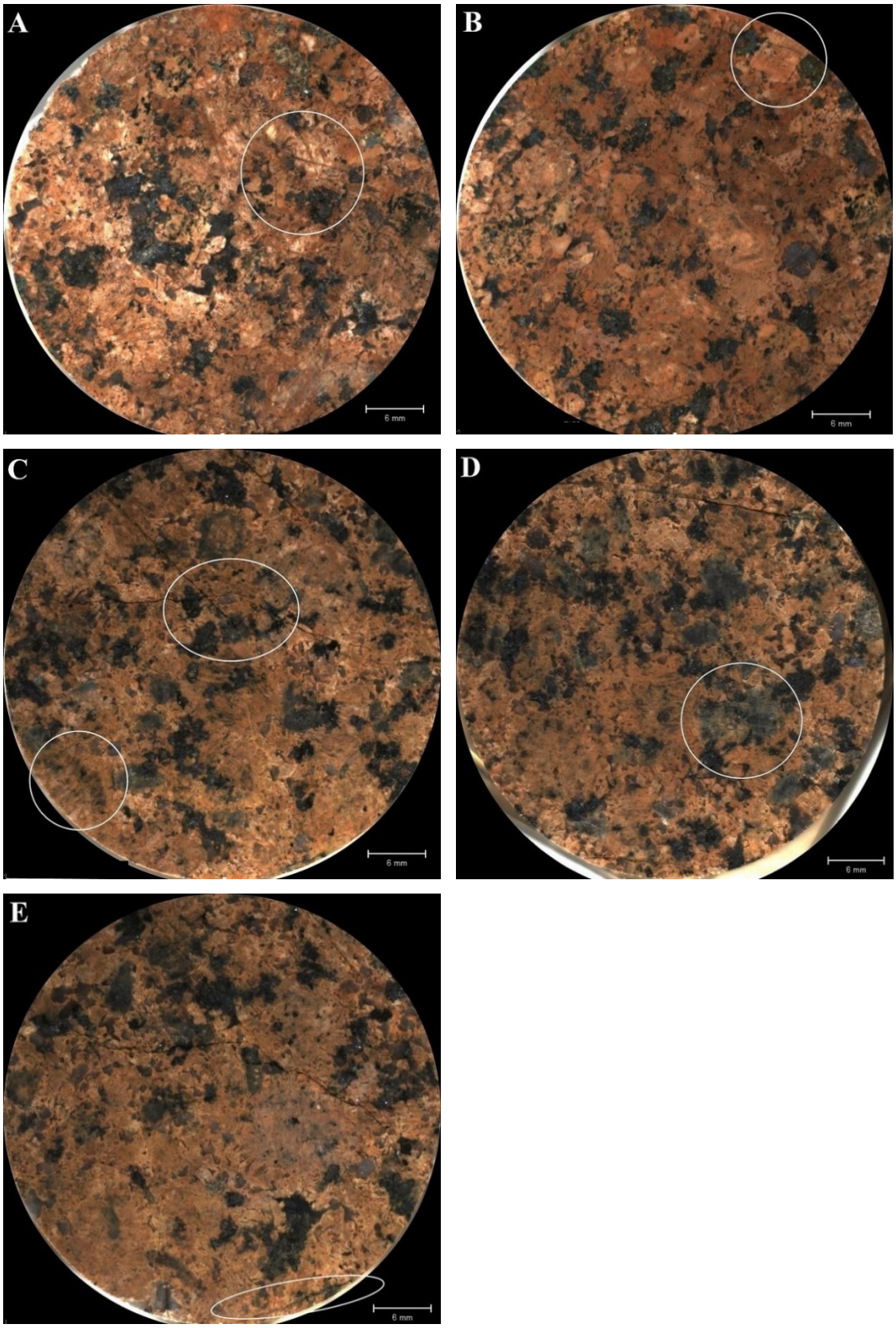

Figure 17: Single sample slices from three different grinding tomography samples (1.1A, 2.1 and 4.1) highlighting certain details which can be observed with this particular resolution, (white circles). North is situated upwards in every picture. A: with NW-SE trending fracture that cross-cut WNW-ESE trending fractures at an angle of approximately of 45°. B: Feldspar lamellae. C: Characterized by fracture forming pattern inside the upper white circle, whereas the lower one is characterized by intercrystalline alteration. D: alteration inside the biotite grain. E: relatively thick quartz vein.

3.3.4 Comparison between grinding tomography and CT-imaging in 2D

Slices of sample 2.1 from the elevation of 38581 microns and 28132 microns were used for comparison of what can be seen in 2D by two different tomography methods. Correlating height and adjustment of images do not match perfectly, as the images were generated by different persons, and the grinding tomography data exist only from 50 microns intervals. However, the images match each other within 100 microns range.

Open joints are very easily detected from both methods, yet slightly more accurate in CT-images, as there are much less color contrasts (Figs. 18 and 19). However, by zooming in the grinding images, same features of open joints can be seen accurately. The differences appear when the small fractures with mineral infills are assessed, as in CT-images they are rather invisible. In figure 19 in the middle/bottom left corner quartz vein is very clearly detected from the grinding image, whereas in the CT-image there is shown only thin outlines, in addition it is impossible to specify the content of the vein by observing the CT-image. The same quartz vein is more clearly detectable from figure 17e. Specifying the minerals and alteration occurring within them is possible in grinding 2D-images but not from CT-images, as the lighter areas are only spots where some sort of spreading of minerals occur that could be interpreted as alteration, more specific definition is not possible. All in all, when observed in 2D, the grinding images show much more detailed view in comparison with CT-scanning (Figs. 18, 19, 17).

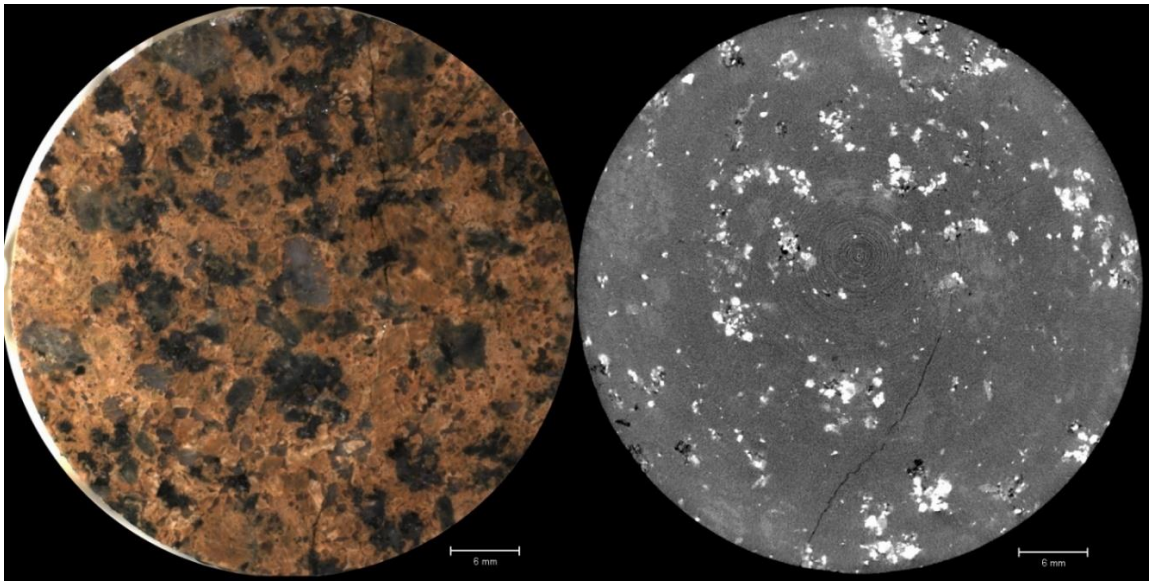

Figure 18: Sample slice of grinding tomography data and CT-scanning image from height of 38581 microns. Grinding tomography image on the left side and CT-image on the right side. The heights do not match perfectly but are in range of 100 microns. North is pointing to the right in the figures.

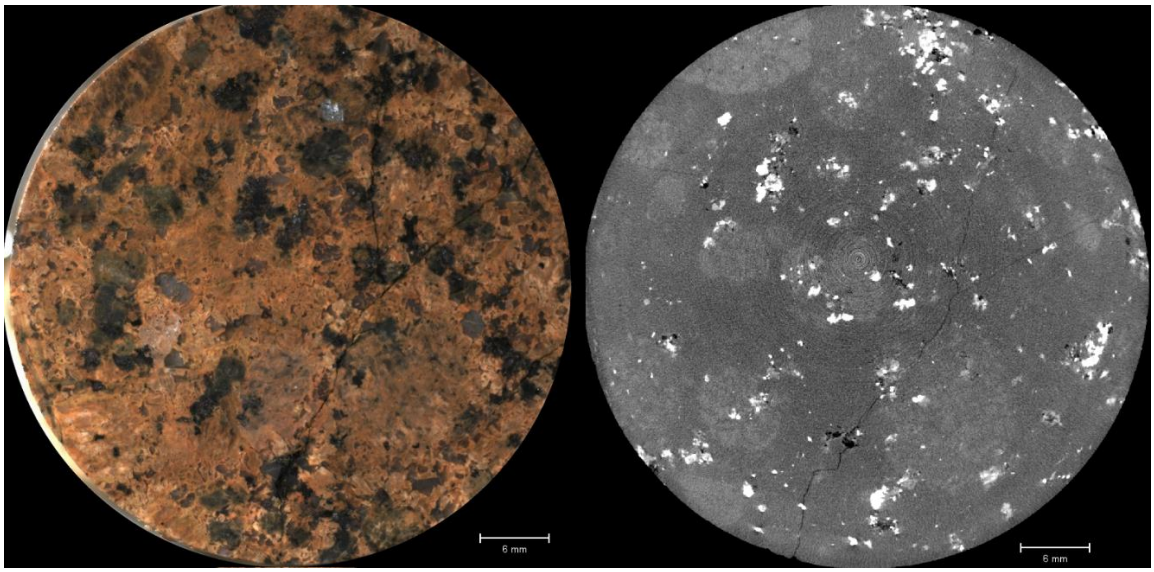

Figure 19: Images from the same sample as in Figure 18. From heights of around 28132 microns, again the heights are in range of 100 microns.

3.3.5 2D topology of 3D-grinding samples (selected slices)

Topology analyses were conducted for two individual grinding tomography samples (1.1A-GETA and 2.1-GETA) as well as for different depths of same samples. Sample 1.1A was analyzed at height of 51835 microns and the other slice within the same sample was from the depth of 18634 microns. Sample 2.1 was analyzed at the heights of 38581 microns and 30700 microns.

3.3.5.1 ***Sample 1.1A-GETA topology***

The results differed by depth, as the sample from upper surface (51835 microns) had more chaotic and more varying fracture patterns. In addition, the fractures were considerably shorter and the connectivity seem to be higher in upper level, as also the amount of fractures were a bit higher (Fig 20). However, the most dominant fracture trend in both slices is the same (WNW-ESE). Sample from lower level (18634 microns) is characterized by NW-SE trending fractures that are considerably longer and more continuous across the sample slice (Fig. 20). The amount of fractures is also lower than in the upper level slice. The connectivity in both samples is quite low, yet it is a lot higher in the upper level sample relative to lower level sample, as the node count for lower level sample is *X*: 2, *Y*: 7 and *I*: 113, whereas other slice has *X*: 6, *Y*: 9 and *I*: 130. Powerlaw exponent in lower slice is 2.972 whereas the higher is 2.488.

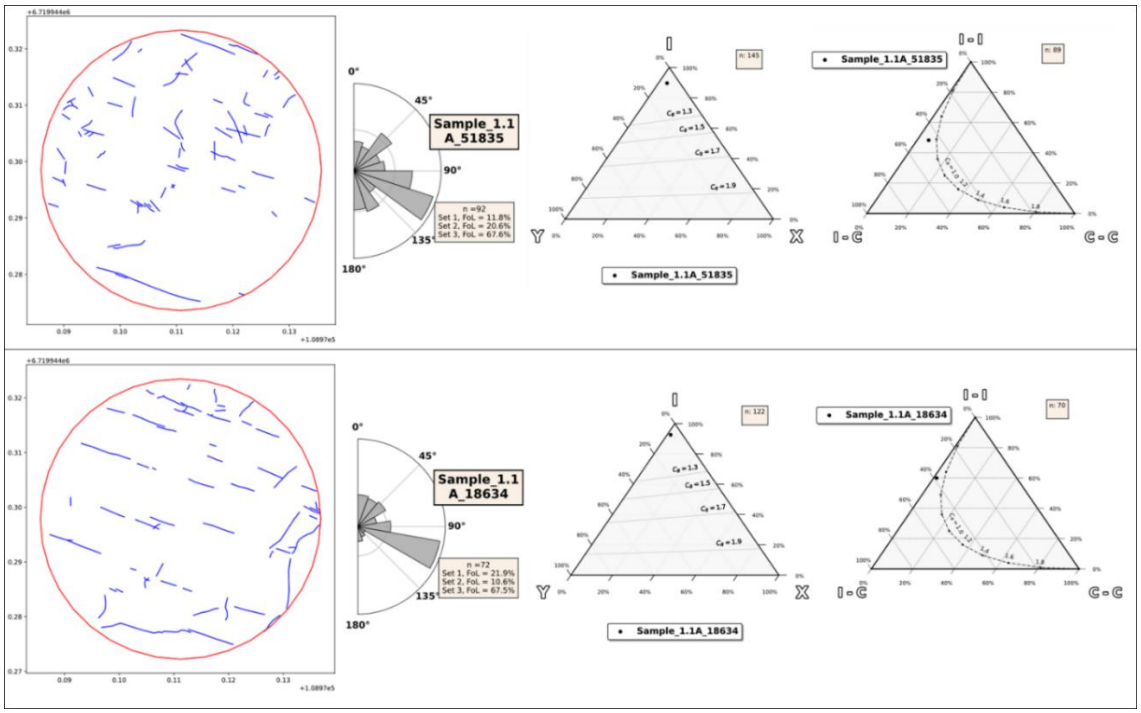

Figure 20. Results of Fractopo analysis conducted in small-scale at two different depths from sample GETA-1.1A. Left to right: fracture traces, rosette plots, XYI and branch diagrams.

3.3.5.2 *Sample GETA-2.1 topology*

The fracture sizes between the slices do not show same kind of variation as in sample 1.1A. Both of the slices are characterized by WNW-ESE trending long continuous fracture, although the continuous fracture in the lower slice (30700 microns) is far more uniform than in the upper (38581 microns) slice. The amount of smaller fractures increases for a bit in lower slice (Fig. 21). However, the more noticeable difference between the short fractures is the variation in their orientation. In upper slice the dominant fracture trend for short fractures is N-S, whereas in the lower slice the short fractures show more variation, the two dominant trends are NW-SE and NE-SW. Powerlaw exponent shows also noticeable difference between the slices, the upper one has powerlaw exponent of 2.138 and lower slice has powerlaw exponent of 1.312.

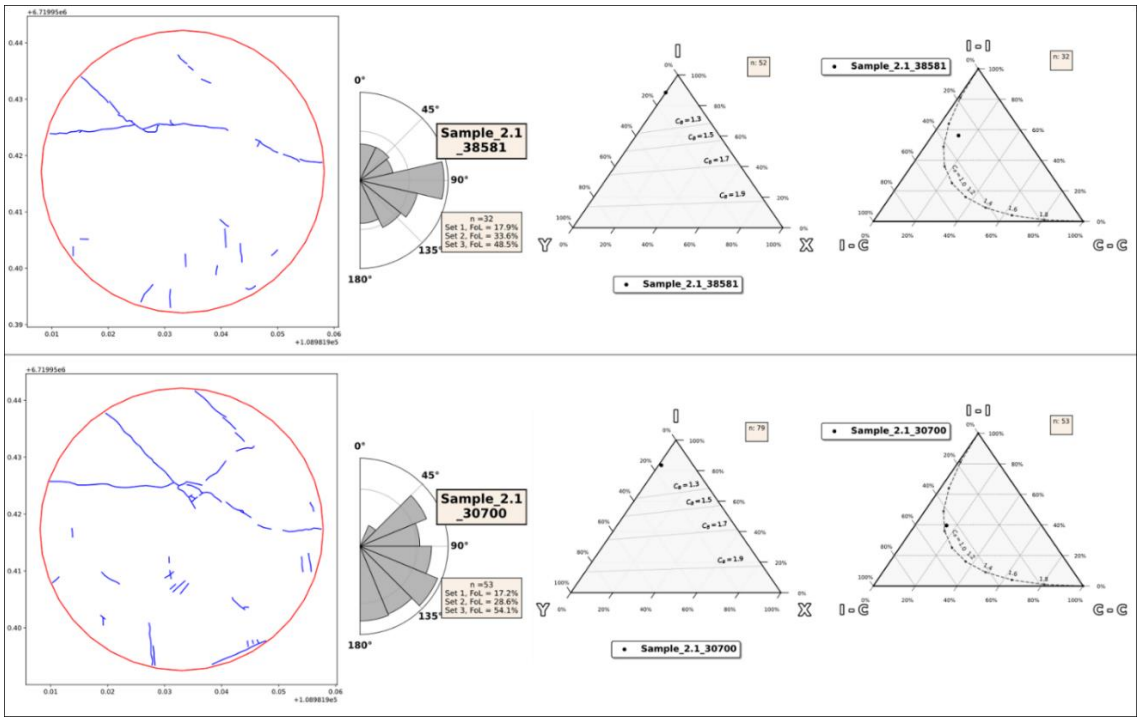

Figure 21. Results of Fractopo analysis conducted in small-scale at two different depths from sample GETA-2.1. Left to right: fracture traces, rosette plots, XYI and branch diagrams.

3.3.5.3 *Comparison of regional versus small-scale topology*

Results correlate each other the most when it comes to NW-SE trending fracture patterns between small-scale fracture patterns compared to footwall side fracturing, as the NW-SE oriented trend is most dominant in small-scale analyses. Fault-parallel NE-SW fracturing occurs also to some extent in the small-scale samples. Particularly, the lower slice of the sample 2.1 shows fault-parallel short fractures that were mostly N-S oriented in the upper slice (Fig. 21). Thus, either one of fault-parallel trends in samples is not the dominating trend. Hanging-wall and fault domains have different fracture patterns compared to the samples, as the dominant trends for the big domains is sub-fault-parallel NEE-SWW. XYI and branch ternary plots show very little variations between the scales.

3.4 MICRON-SCALE 3D-MODELLING OF FAULT-INDUCED SECONDARY FRACTURING

3D-modelling of fault-induced secondary fracturing was conducted from sample GETA-2.1-2020. Modelling of fractures was based on fracture trace lines digitized on various slices of grinding tomography images. A total of 9 individual images were used with 1 mm intervals. The model was scaled so that 1 kilometer in MOVE equals to 1 cm in real life, as the sample size is 5*5 cm, i.e. in the z axis 100 meters equals to 1 mm in real life.

3.4.1 3D-model

3D-model represents three Mode I fractures (Figs. 22 and 23). One is isolated and two others represent cross-cutting fractures. Model was conducted in MOVE, so acquiring the orientation data of the fractures was also possible. Dipdir/dip of the isolated cyan-colored fracture is 043/55 and the other cyan-colored cross-cutting fracture is oriented 045/58. The other cyan colored fracture cross-cuts the red fracture at angle of approximately 45°. Orientations of these particular fractures are compatible with the macro-scale damage zone fracture orientations from the wall damage zone where the sample 2.1 was taken (Fig. 13; "IV": Section 3.1). Cyan-colored fractures are relatively planar, whereas the third (red) fracture is rather curved. The third fracture is oriented 178/83 in its western part but after the cross-cutting cyan colored fracture in the east, its mean orientation changes to 197°/62° and geometry becomes more curved than planar, and the dip becomes more gentle. The red-colored fracture is also compatible with orientations measured in macro-scale damage zone fracturing (Fig. 13; "IV": Section 3.1).

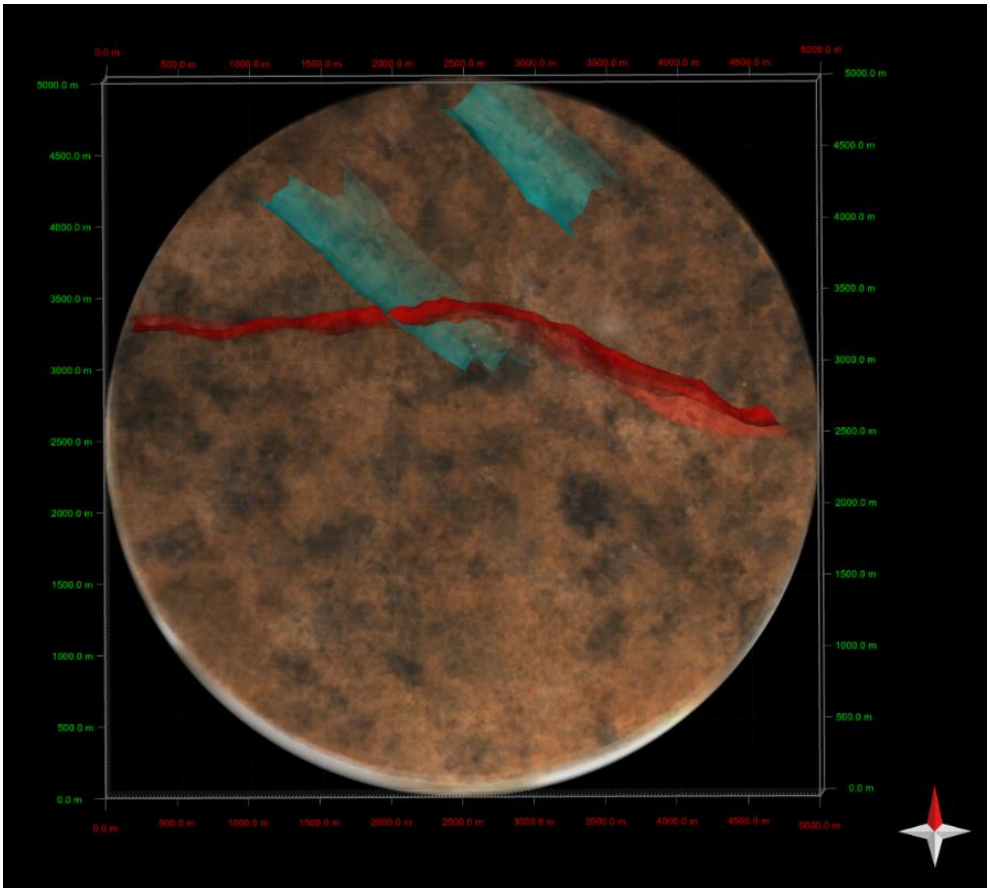

Figure 22. 3D-model of the fractures in sample GETA-2.1-2020. View from above. 1:10 000.

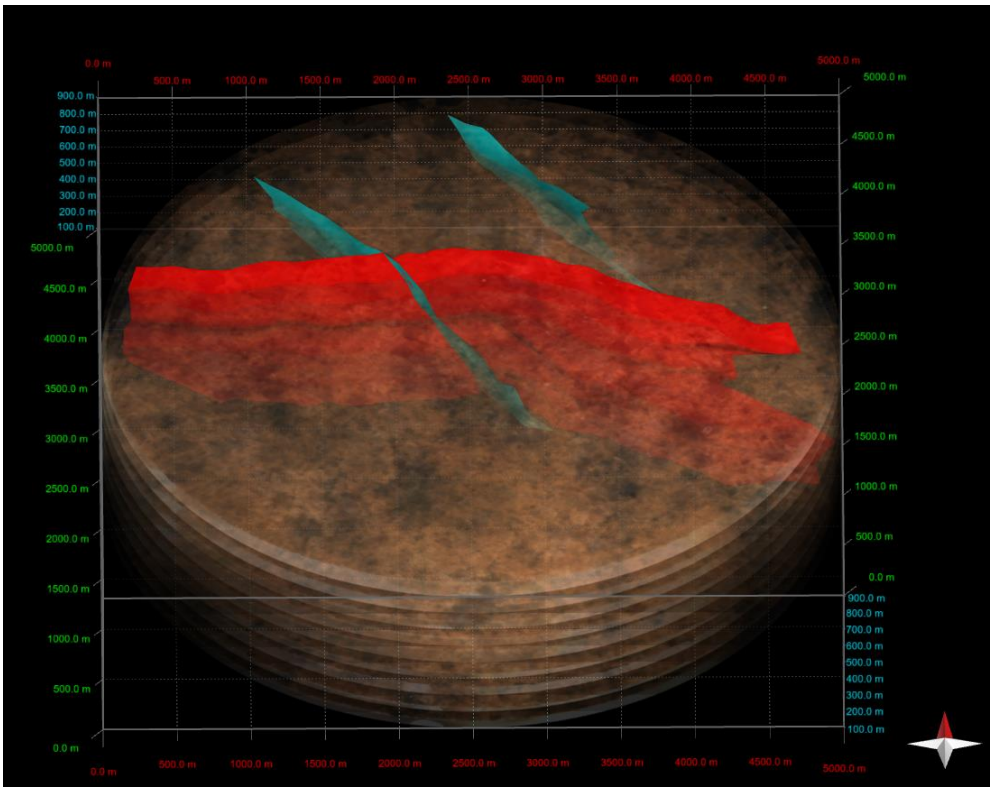

Figure 23. 3D-model of sample GETA-2.1-2020 Mode I micro-fractures. Image from perspective view. On X and Y axis the scale is 1:10 000 as 1000 meters equals to 1 cm and on Z axis scale is 1:1000 where 100 meters equals to 1 mm.

4 DISCUSSION

4.1 FAULT GEOMETRY EFFECTS ON FAULT-INDUCED FRACTURING

Field observations together with the virtual mapping reveals that the fracturing intensity variation is coupled with variation in fault geometry when observed in larger scale, whereas in small-scale fracture intensity shows no significant variation between different DZs. In macro-scale the fracturing is most intense in areas of wall, -linking and tip damage zones, and relatively sparse in fault bend damage zone (Fig. 13; "I-V"). The sparse fracturing occurring in fault bend damage zone may be due to the restraining step-over and extensional releasing bend characteristics, which are known as paired bends when occurring adjacent (Cunningham and Mann, 2007). In these cases, less fractures form due to the prevailing stress orientations. However, typically similar structures are known to be complex sites of fracturing and possible fluid flow (Cunningham and Mann, 2007) yet the topology analyses conducted on this Thesis, show no significant variation at any scale (Section 3.2). These types of fault features are typically accommodated by oblique deformation, for example, the oblique slip faulting either partitioned components

of strike-slip and dip-slip displacements (Jones and Tanner, 1995), which is essentially compatible with the minor reverse component of slip occurring in the Geta fault.

4.2 DAMAGE ZONE EXTENDING BEYOND PREDICTED SCALING-LAW BOUNDARIES

The Geta fault is situated within mesoscopically isotropic homogenous rapakivi granite in the Northernmost region of the Åland, Finland. Due to the 3D character of the fault, it offers a possibility to study its 3D-geometry and fracture network, which is typically challenging in Finland due to flat topography. The Geta fault is overall compatible to strike-slip regime, as it is characterized by clearly identifiable features of strike-slip fault, such as sub-horizontal lineations and subsidiary fracture patterns. In addition, the fault has a minor reverse component of slip. Moreover, the fault is characterized by well-developed distinct damage zones with patterns of secondary fractures. The damage zone extends seemingly so far on footwall side that it is out of generally known scaling-law boundaries (Faulkner et al., 2011). However, DZs above scaling-laws could be explained by interaction of several faults (Kim et al., 2004; Peacock et al., 2017). As the South-Eastern parts of study area is associated with at least one additional strike-slip fault, which strikes in similar direction as Geta fault and correlates also with the sense-of-movement. Furthermore, the fracturing intensity and orientation seems to correlate with the damage zone fracturing close to the Geta fault. Particularly, the coastline vicinity seems to be affected the most by the faulting, thus the damage zone seems to be continuous beyond the study area, which may also host more faults that interact with known faults. The possibility of a DZ that exceeds typical scaling-laws is also supported by the previous studies conducted in the corresponding isotropic Rapakivi batholith in Orrengrund, Finland, where the study area is associated with wide DZs that are extending beyond the predicted scaling-law boundaries (Skyttä et al., 2021). Although, the fracture intensity shows very little variation across the Geta study area, whereas according to Ostermeijer et al. 2020, interaction of several faults tends to lead more varying fracture intensities.

It has been established here that the Geta fault clearly serves as a distinguishing factor between the Hanging-wall and footwall fracture orientations within the Geta study area (Figs. 12 and 13). It is likely that faulting has not affected the hanging-wall side fracturing of the fault as much as in footwall, as the hanging-wall side is seemingly characterized with regional fracturing, even though the hanging-wall accommodates one clear fault-parallel fracture set. By contrast, the NW-SE oriented fracturing is minor, which is the

main orientation of damage zone fracturing within the footwall. The long continuous NNE-SSW fractures across the study area also show small variation in their orientation as with in the footwall they are distributed more NE-SW, whereas in the hanging-wall side they are clearly oriented more towards N-S (Fig. 12), which may also be caused by the faulting.

4.3 ANALYZING TOPOLOGY FROM GRINDING TOMOGRAPHY DATA

2D topology analyses were conducted from the study area based on manually digitized fracture traces and the same methodology was applied to the grinding tomography data. The analyses were based on using topology parameters nodes and branches (Sanderson and Nixon, 2015). The results show variations depending on the analyzed surface especially in trace length distributions, fracture frequency and in orientations. However, in ternary plots, the results show also very little variation (Figs. 14, 20 and 21) in both observed scales. Analyzing topology is often limited to 2D, thus the grinding tomography data provides the means for studying 3D-connectivity of fractures, although in this Thesis the method was only applied to two individual slices of different depths in 2D (Figs. 20 and 21). Grinding tomography has been previously utilized to study the structures of fossils (Pascual-Cebrian et al., 2013), whereas the X-ray methods have been previously utilized in studies related to fractures (e.g, Nasseri et al., 2011). Both grinding tomography and X-ray based methods e.g. CT-scanning provide the means for topology-based characterization of three-dimensional samples (Sanderson and Nixon, 2015). Whereas the preservative X-ray methods utilize the density differences in internal composition of materials (Pascual-Cebrian et al., 2013), grinding tomography allows detecting structures e.g., open mode fractures which are not density dependent, such as fractures that are filled by material with same density as the surrounding material (e.g. Figures 18 and 19). Results of topology analyses would vary significantly when assessed between these two methods, since the filled fractures are invisible in CT images on these particular samples. Utilizing grinding tomography method to study topology characteristics of micro-fractures isn't a certainty. Method encounters similar problems as for example, borehole and well connectivity studies, as the length-scale of fractures could be greater than diameter of the studied object (Sanderson and Nixon, 2015). However, Özkaya (2003) suggest that estimations of the length-scale of fractures is possible based on the relative frequency of complete fracture traces.

4.4 RELATIONSHIP BETWEEN FAULT AND MICRO-FRACTURING

Due to polyphase deformation, accurate and precise determinations of fault and fracture age relations is impossible (Peacock, 2001). However, according to the conceptual model of the brittle evolution of southwestern Finland (Mattila and Viola, 2014) the formation of Geta fault may date between the paleostress stages 5-7, and especially to the stage 6, when the orientation of the compressional stress tensor was WNW-ESE (Mattila and Viola, 2014).

The micro-fractures could pre-date the faulting, and thus create a weak orientation for the fault propagation due a coalescence of micro-fractures (Kranz, 1983, Anders et al., 2014, Crider, 2015) (Fig 4; Section 1.31, 1.32). However, the orientations of modelled micro-fractures of this study imply that they are fault-induced rather than pre-existing micro-fracturing, as the orientations are compatible with the measured orientations of macro-scale DZ fracturing. In fact, the parallelism between micro-fractures and macrofractures is shown in many studies (e.g. Vermilye and Scholz, (1998); Laubach and Diaz-Tushman, (2009) as the nucleation of micro-fracturing occurs in grain scale and the micro-fractures may further propagate so that they become macrofractures (Kranz, 1983, Anders et al., 2014, Crider, 2015). Moreover, according to Laubach (1989) fractures that belong to the same sets commonly have corresponding orientations in different scales.

4.4.1 3D-model of micro-fractures

Two out of three modelled fractures have relatively gentle dips 55° and 58° (Figs. 22 and 23), compatible with measurements taken in field, whereas the third micro-scale damage zone fracture had a steeper dip 83°, which essentially changed towards more gently dipping (62°) after the intersection with another fracture (Figs. 22 and 23). The steeper dipping fracture is more compatible with existing models of secondary fracturing, as Martel and Boger (1998) measured dips 80° and higher from crystalline granites, whereas Skyttä et al (2021) defined average dips approximately 70° from the corresponding rock type for wing-cracks. Although, the variation in fracture dips and their geometry may simply alter according to the initial stress state. However, in macro-scale the damage zone fracturing was planar as it was also pointed out by Martel and Boger (1998), however in micro-scale one out of three fractures was curved (Figs. 22 and 23). At first the curved fracture had planar characteristics but after intersection with another fracture, geometry changed towards more curved and twisted.

No micro-fracture data was derived away from the fault surface, yet the micro-fracture density was far less than expected, even though the samples were taken from the vicinity of slip surface, whereas in many studies (e.g. Brock and Engelder, 1977; Chester and Logan, 1986) micro-fracture density increases as the fault surface is approached, which has supported the models where the studied faults have grown by coalescence of micro-fractures. Whether the stress would have affected the Geta fault from same orientations as before, the studied micro-fractures would eventually coalescence into macro-scale damage zone fracturing with comparable orientations to existing damage zone fracturing.

4.5 SOURCES OF ERROR IN THE TOPOLOGY DATASETS

Results from the regional topology analyses show very little variation when assessing the node and branch data between hanging-wall, footwall and the fault vicinity, as the results plot close to a same (Figs. 14, 20 and 21.) Especially the analyses from the fault vicinity will most likely have inaccurate results, as the outcrops in the area were not planar, particularly within the vicinity of the Geta fault on footwall side, where the outcrop was comparatively steep. Thus, caused topographical problems when assessing the orthomosaics, which further leads to uncertainties and distorted interpretations in the most essential parts of the damage zones around fault, as well as in the certain parts of the study area. Digitization of fracture traces has also other issues related to fracture interpretations. Because of the resolution limited to pixel size of 0.55 cm, there will most likely occur inaccurate interpretations related to connectivity of traces. In certain parts due to outcrop shading there is no possibility to make an accurate interpretation when it comes to trace connectivity. Also, results could vary slightly depending on the digitizer, especially with limited resolution the decisions are subjective when it comes to interpretations in certain parts of the study area. Although, as this work had only one person to digitize the traces, it may cut off some variability.

4.5.1 Exploitation of machine learning and artificial intelligence in fracture detection

In future, machine learning and artificial intelligence image pattern recognition can be the key for cutting off the distorted interpretations made by human and in addition save countless working hours in the field of engineering geology as well as in a variety of other engineering and scientific fields such as medicine and biology. However, despite years of research and development, the main problem of recognizing complex image patterns e.g. fractures with arbitrary orientation, location and scale remain unsolved (Basu et al.,

2010). Automated fracture dectection has been also under research in MIRA-3D project by University of Turku PET-center and GTK, yet the accuracy of recognizing the fractures is not yet at a desired level, one of the key problems being the limited resolution of the used data. Although, semi-automatic tools were applied on this Thesis by using CloudCompare software (Girardeau-Montaut, 2015) compass plugin plane and trace tools (Thiele et al., 2017) in certain planes and fractures, which were first visually detected from the point cloud data. For example, the trace tool applies least-cost-path algorithm (Fig. 8) which provides an estimate of the fracture trace by brightness-based cost function that results in low-cost edges between adjacent points and pixels that both belong on the fracture trace (Thiele et al., 2017). The approach has been previously utilized to detect linear features in a wide range of image data and proven reliable even with 'bad quality' data (e.g., Vincent, 1998; Sun and Pallottino, 2003). As the fault was mapped both virtually and traditionally in the field, small comparison was conducted of the virtually mapped results versus field measurements. Evaluation was made based on three different measurements: fault splay branch from NE termination was manually measured 339/58, whereas virtually the result was 322/64. Measurement from linking damage zone fracturing was in the field 278/77 and virtually 272/82, fault surface was measured 336/70 in field and 336/71 virtually. The result show small but acceptable variations that may be caused, for example by natural surface roughness (Dewez et al., 2016). Only three measurements were chosen for this evaluation as this topic has been discussed and evaluated by several researches (e.g., Dewez et al., 2016; Sayab et al., 2018).

5 CONCLUSIONS

- The grinding tomography method allows to generating data based on which microstructures can be modeled and observed with micrometer accuracy. The method provides the means for evaluating the relationship between faults and fault-related secondary fracturing and fault kinematics at variable scales.
- The method also provides means for analyzing topology in micron-scale.
- Grinding tomography images are accurate and many different details can be viewed from them, such as intercrystalline fracturing and alteration. The grinding tomography data seems to provide more detail in 2D sections than CT-images of corresponding samples.
- Geta fault effects on the fracture orientations in the study area.

- Damage zone in the Geta footwall exceeds the known scaling-law boundaries.
- Orientations and dips of the micro-scale secondary fracturing corresponds to the macro-scale fracturing within the damage zone.
- In micro-scale, fracture intersections affect the fracture geometries, whereas in larger scale the corresponding phenomena is not observed.
- Fracturing intensity variation is coupled with variation in the fault geometry when observed in larger scale, whereas in small-scale fracture intensity show no variation between geometry variations.

6 ACKNOWLEDGEMENTS

To begin with, I would like to thank VYR (Valtion Ydinjätehuoltorahasto) for funding the MIRA-3D project, and KARIKKO project for nice collaboration. Working on this Thesis has been instructive and rewarding, thanks to my supervisor Professor Pietari Skyttä from the University of Turku. Furthermore, I would like to express my gratitude to Nicklas Nordbäck, GTK, for providing drone acquired data used in this Thesis. I would also like to thank Jukka Kuva, GTK, for CT-scanning the samples and for his valuable expertise on the matter. Additionally, I would like to thank MSc Nikolas Ovaskainen, GTK, for helping with the topology analyses.

REFERENCES

Achtziger-Zupančič, P., Loew, S., Hiller, A., & Mariethoz, G. 2016: 3D fluid flow in fault zones of crystalline basement rocks (Poehla-Tellerhaeuser Ore Field, Ore Mountains, Germany). *Geofluids*, *16*(4), 688-710.

Agisoft, **2018:** Agisoft PhotoScan User Manual: Professional Edition. Copyright © 2018 Agisoft LLC 127.

Anders, M. H., Laubach, S. E., & Scholz, C. H. 2014: Microfractures: A review. *Journal of Structural Geology*, *69*, 377-394.

Andersson, H. I., Bech, K. H., & Dandapat, B. S. 1992: Magnetohydrodynamic flow of a power-law fluid over a stretching sheet. *International Journal of Non-Linear Mechanics*, *27*(6), 929-936.

Aydin, A. 2000: Fractures, faults, and hydrocarbon entrapment, migration and flow. *Marine and petroleum geology*, *17*(7), 797-814.

Basu, J. K., Bhattacharyya, D., & Kim, T. H. 2010: Use of artificial neural network in pattern recognition. *International journal of software engineering and its applications*, *4*(2).

Barnett, J. A., Mortimer, J., Rippon, J. H., Walsh, J. J., & Watterson, J. 1987: Displacement geometry in the volume containing a single normal fault. *AAPG Bulletin*, *71*(8), 925-937.

Bastesen, E., & Rotevatn, A. 2012: Evolution and structural style of relay zones in layered limestone–shale sequences: insights from the Hammam Faraun Fault Block, Suez rift, Egypt. *Journal of the Geological Society*, *169*(4), 477-488.

Berkowitz, B. 2002: Characterizing flow and transport in fractured geological media: A review. *Advances in water resources*, *25*(8-12), 861-884.

Bilham, R., & King, G. 1989: The morphology of strike-slip faults: Examples from the San Andreas Fault, California. *Journal of Geophysical Research: Solid Earth*, *94*(B8), 10204-10216.

Billi, A., Salvini, F., & Storti, F. 2003: The damage zone-fault core transition in carbonate rocks: implications for fault growth, structure and permeability. *Journal of Structural geology*, *25*(11), 1779-1794.

Bobet, A. 2000: The initiation of secondary cracks in compression. *Engineering Fracture Mechanics*, *66*(2), 187-219.

Bonnet, E., Bour, O., Odling, N. E., Davy, P., Main, I., Cowie, P., & Berkowitz, B. 2001: Scaling of fracture systems in geological media. *Reviews of geophysics*, *39*(3), 347-383.

Brace, W. F., Paulding Jr, B. W., & Scholz, C. H. 1966: Dilatancy in the fracture of crystalline rocks. *Journal of Geophysical Research*, *71*(16), 3939-3953

Brogi, A., Fabbrini, L., & Liotta, D. 2011: Sb–Hg ore deposit distribution controlled by brittle structures: the case of the Selvena mining district (Monte Amiata, Tuscany, Italy). *Ore Geology Reviews*, *41*(1), 35-48.

Brock, W. G., & Engelder, T. 1977: Deformation associated with the movement of the Muddy Mountain overthrust in the Buffington window, southeastern Nevada. *Geological Society of America Bulletin*, *88*(11), 1667-1677.

Caine, J. S., Evans, J. P., & Forster, C. B. 1996: Fault zone architecture and permeability structure. *Geology*, *24*(11), 1025-1028.

Caine, J. S., & Forster, C. B. 1999: Fault zone architecture and fluid flow: Insights from field data and numerical modeling. *Geophysical Monograph-American Geophysical Union*, *113*, 101-128

Chester, F. M., & Logan, J. M. 1986: Implications for mechanical properties of brittle faults from observations of the Punchbowl fault zone, California. *Pure and applied geophysics*, *124*(1), 79-106.

Chester, F. M., Chester, J. S., Kirschner, D. L., Schulz, S. E., & Evans, J. P. 2004: 8. Structure of Large-Displacement, Strike-Slip Fault Zones in the Brittle Continental Crust. In *Rheology and Deformation of the Lithosphere at Continental Margins* (pp. 223-260). Columbia University Press.

Childs, C., Manzocchi, T., Walsh, J. J., Bonson, C. G., Nicol, A., & Schöpfer, M. P. 2009: A geometric model of fault zone and fault rock thickness variations. *Journal of Structural Geology*, *31*(2), 117-127.

Choi, J. H., Edwards, P., Ko, K., & Kim, Y. S. 2016: Definition and classification of fault damage zones: A review and a new methodological approach. *Earth-Science Reviews*, *152*, 70-87.

Christie-Blick, N., & Biddle, K. T. 1985: Deformation and basin formation along strike-slip faults.

Conroy, G. C., & Vannier, M. W. 1984: Noninvasive three-dimensional computer imaging of matrix-filled fossil skulls by high-resolution computed tomography. *Science*, *226*(4673), 456-458.

Cowie, P. A., & Scholz, C. H. 1992: Displacement-length scaling relationship for faults: data synthesis and discussion. *Journal of Structural Geology*, *14*(10), 1149-1156.

Crider, J. G., & Pollard, D. D. 1998: Fault linkage: Three-dimensional mechanical interaction between echelon normal faults. *Journal of Geophysical Research: Solid Earth*, *103*(B10), 24373-24391.

Crider, J. G., & Peacock, D. C. 2004: Initiation of brittle faults in the upper crust: a review of field observations. *Journal of Structural Geology*, *26*(4), 691-707.

Crider, J. G. 2015: The initiation of brittle faults in crystalline rock. *Journal of Structural Geology*, *77*, 159-174.

Cunningham, W. D., & Mann, P. (2007): Tectonics of strike-slip restraining and releasing bends. *Geological Society, London, Special Publications*, *290*(1), 1-12.

Dewez, T. J., Girardeau-Montaut, D., Allanic, C., & Rohmer, J. 2016: FACETS: A CLOUDCOMPARE PLUGIN TO EXTRACT GEOLOGICAL PLANES FROM UNSTRUCTURED 3D POINT CLOUDS. *International Archives of the Photogrammetry, Remote Sensing & Spatial Information Sciences*, *41*.

Dyskin, A. V., Germanovich, L. N., & Ustinov, K. B. 1999: A 3-D model of wing crack growth and interaction. *Engineering Fracture Mechanics*, *63*(1), 81-110.

Ehlers, C., & Bergman, L. 1984: Structure and mechanism of intrusion of two postorogenic granite massifs, southwestern Finland. In *Precambrian tectonics illustrated* (pp. 173-190).

Elo, S., & Korja, A. (1993): Geophysical interpretation of the crustal and upper mantle structure in the Wiborg rapakivi granite area, southeastern Finland. *Precambrian Research*, *64*(1-4), 273-288.

Faulkner, D. R., Jackson, C. A. L., Lunn, R. J., Schlische, R. W., Shipton, Z. K., Wibberley, C. A. J., & Withjack, M. O. 2010: A review of recent developments concerning the structure, mechanics and fluid flow properties of fault zones. *Journal of Structural Geology*, *32*(11), 1557-1575.

Griffith, A. A. 1921: VI. The phenomena of rupture and flow in solids. *Philosophical transactions of the royal society of london. Series A, containing papers of a mathematical or physical character*, *221*(582-593), 163-198.

Griffith, A. 1924: The theory of rupture. In *First Int. Cong. Appl. Mech* (pp. 55-63).

Granier, T. 1985: Origin, damping, and pattern of development of faults in granite. *Tectonics*, *4*(7), 721-737.

Griggs, D. T., & Handin, J. 1960: Rock deformation.

Haapala, I., & Rämö, O. T. 1990: Petrogenesis of the Proterozoic rapakivi granites of Finland. *Geological Society of America Special Paper*, *246*, 275-286.

Hancock, J. W., & Thomson, R. D. 1985: Strain and stress concentrations in ductile fracture by void nucleation growth and coalescence. *Materials science and technology*, *1*(9), 684-690.

Hoek, E., & Brown, E. T. 1997: Practical estimates of rock mass strength. *International journal of rock mechanics and mining sciences*, *34*(8), 1165-1186.

Hounsfield, G. N. 1980: Computed medical imaging. *Medical physics*, *7*(4), 283-290.

Horii, H., & Nemat-Nasser, S. 1986: Brittle failure in compression: splitting faulting and brittle-ductile transition. *Philosophical Transactions of the Royal Society of London. Series A, Mathematical and Physical Sciences*, *319*(1549), 337-374.

Ishii, E. 2016: Far-field stress dependency of the failure mode of damage-zone fractures in fault zones: Results from laboratory tests and field observations of siliceous mudstone. *Journal of Geophysical Research: Solid Earth*, *121*(1), 70-91.

Ito, T., & Zoback, M. D. 2000: Fracture permeability and in situ stress to 7 km depth in the KTB scientific drillhole. *Geophysical Research Letters*, *27*(7), 1045-1048.

Janecke, S. U., Dorsey, R. J., Steely, A. N., Kirby, S. M., Lutz, A., Housen, B. A., ... & Forand, D. 2008: High geologic slip rates since Early Pleistocene initiation of the San Jacinto and San Felipe Fault zones in the San Andreas fault system, paper presented at Annual Meeting. *South. Calif. Earthquake Cent., Palm Springs, Calif*.

Jing, L., & Stephansson, O. 1997: Network topology and homogenization of fractured rocks. In *Fluid flow and transport in rocks* (pp. 191-202). Springer, Dordrecht.

Jones, R. R., & Tanner, P. G. 1995: Strain partitioning in transpression zones. *Journal of Structural Geology*, *17*(6), 793-802.

Karell, F., Ehlers, C., & Airo, M. L. 2014: Emplacement and magnetic fabrics of rapakivi granite intrusions within Wiborg and Åland rapakivi granite batholiths in Finland. *Tectonophysics*, *614*, 31-43.

Kim, Y. S., Andrews, J. R., & Sanderson, D. J. 2001: Reactivated strike–slip faults: examples from north Cornwall, UK. *Tectonophysics*, *340*(3-4), 173-194.

Kim, Y. S., & Sanderson, D. J. 2006: Structural similarity and variety at the tips in a wide range of strike–slip faults: a review. *Terra Nova*, *18*(5), 330-344.

Kim, Y. S., & Sanderson, D. J. 2008: Earthquake and fault propagation, displacement and damage zones. *Structural Geology: New Research*, *1*, 99-117.

Kranz, R. L. (1983): Microcracks in rocks: a review. *Tectonophysics*, *100*(1-3), 449-480.

Kurt, H., Sorlien, C. C., Seeber, L., Steckler, M. S., Shillington, D. J., Cifci, G., ... & Carton, H. 2013: Steady late quaternary slip rate on the Cinarcik section of the North Anatolian fault near Istanbul, Turkey. *Geophysical Research Letters*, *40*(17), 4555-4559.

Lajtai, E. Z. 1971: A theoretical and experimental evaluation of the Griffith theory of brittle fracture. *Tectonophysics*, *11*(2), 129-156.

Laubach, S. E., Lander, R. H., Criscenti, L. J., Anovitz, L. M., Urai, J. L., Pollyea, R. M., ... & Pyrak-Nolte, L. 2019: The role of chemistry in fracture pattern development and opportunities to advance interpretations of geological materials. *Reviews of Geophysics*, *57*(3), 1065-1111.

Lunn, R. J., Shipton, Z. K., & Bright, A. M. 2008: How can we improve estimates of bulk fault zone hydraulic properties *Geological Society, London, Special Publications*, *299*(1), 231-237.

Manzocchi, T. 2002: The connectivity of two-dimensional networks of spatially correlated fractures. *Water Resources Research*, *38*(9), 1-1.

Maerten, L., Gillespie, P., & Pollard, D. D. 2002: Effects of local stress perturbation on secondary fault development. *Journal of Structural Geology*, *24*(1), 145-153.

Mattila, J., & Viola, G. 2014: New constraints on 1.7 Gyr of brittle tectonic evolution in southwestern Finland derived from a structural study at the site of a potential nuclear waste repository (Olkiluoto Island). *Journal of Structural Geology*, *67*, 50-74.

Martel, S. J., & Boger, W. A. 1998: Geometry and mechanics of secondary fracturing around small three-dimensional faults in granitic rock. *Journal of Geophysical Research: Solid Earth*, *103*(B9), 21299-21314.

McCaig, A. M. 1988: Deep fluid circulation in fault zones. *Geology*, *16*(10), 867-870.

Mutlu, O., & Pollard, D. D. 2008: On the patterns of wing cracks along an outcrop scale flaw: A numerical modeling approach using complementarity. *Journal of Geophysical Research: Solid Earth*, *113*(B6).

Mitchell, T. M., & Faulkner, D. R. 2008: Experimental measurements of permeability evolution during triaxial compression of initially intact crystalline rocks and implications for fluid flow in fault zones. *Journal of Geophysical Research: Solid Earth*, *113*(B11).

Nasseri, M. H. B., Rezanezhad, F., & Young, R. P. 2011: Analysis of fracture damage zone in anisotropic granitic rock using 3D X-ray CT scanning techniques. *International Journal of Fracture*, *168*(1), 1-13.

Naylor, M. A., Mandl, G. T., & Supesteijn, C. H. K. 1986: Fault geometries in basement-induced wrench faulting under different initial stress states. *Journal of structural geology*, *8*(7), 737-752.

Nironen, M. 1997: The Svecofennian Orogen: a tectonic model. *Precambrian Research*, *86*(1-2), 21-44.

Ostermeijer, G. A., Mitchell, T. M., Aben, F. M., Dorsey, M. T., Browning, J., Rockwell, T. K., ... & Ostermeijer, F. 2020: Damage zone heterogeneity on

seismogenic faults in crystalline rock; a field study of the Borrego Fault, Baja California. *Journal of Structural Geology*, *137*, 104016.

Pascual-Cebrian, E., Hennhöfer, D. K., & Götz, S. 2013: 3D morphometry of polyconitid rudist bivalves based on grinding tomography. *Facies*, *59*(2), 347-358.

Peacock, D. C. P., Dimmen, V., Rotevatn, A., & Sanderson, D. J. 2017: A broader classification of damage zones. *Journal of Structural Geology*, *102*, 179-192.

Peacock, D. C. P., Sanderson, D. J., & Rotevatn, A. 2018: Relationships between fractures. *Journal of Structural Geology*, *106*, 41-53.

Petit, J. P., & Barquins, M. 1988: Can natural faults propagate under mode II conditions? *Tectonics*, *7*(6), 1243-1256.

Ramsey, J. M., & Chester, F. M. 2004: Hybrid fracture and the transition from extension fracture to shear fracture. *Nature*, *428*(6978), 63-66.

Rotevatn, A., & Fossen, H. 2011: Simulating the effect of subseismic fault tails and process zones in a siliciclastic reservoir analogue: Implications for aquifer support and trap definition. *Marine and Petroleum Geology*, *28*(9), 1648-1662.

Riquelme, A., Del Soldato, M., Tomás, R., Cano, M., Bordehore, L. J., & Moretti, S. 2019: Digital landform reconstruction using old and recent open access digital aerial photos. *Geomorphology*, *329*, 206-223.

Rämö, O. T., & Haapala, I. 2005: Rapakivi granites. In *Developments in Precambrian Geology* (Vol. 14, pp. 533-562). Elsevier.

Sanderson, D. J., & Nixon, C. W. 2015: The use of topology in fracture network characterization. *Journal of Structural Geology*, *72*, 55-66.

Sayab, M., Suuronen, J. P., Hölttä, P., Aerden, D., Lahtinen, R., & Kallonen, A. P. 2015: High-resolution X-ray computed microtomography: A holistic approach to metamorphic fabric analyses. *Geology*, *43*(1), 55-58.

Sayab, M., Aerden, D., Paananen, M., & Saarela, P. 2018: Virtual structural analysis of jokisivu open pit using 'structure-from-motion'unmanned aerial vehicles (UAV) photogrammetry: Implications for structurally-controlled gold deposits in southwest Finland. *Remote Sensing*, *10*(8), 1296.

Scholz, C. H. 1989: Mechanics of faulting. *Annual Review of Earth and Planetary Sciences*, *17*, 309-334.

Schreurs, G., & Hanni, R. 1998: 4-D analysis of analogue model experiments. *American Association of Petroleum Geologists Bulletin*, *82*(10), 1965.

Sibson, R. H. 1989: Earthquake faulting as a structural process. *Journal of structural geology*, *11*(1-2), 1-14.

Siren, T., Hakala, M., Valli, J., Kantia, P., Hudson, J. A., & Johansson, E. 2015: In situ strength and failure mechanisms of migmatitic gneiss and pegmatitic granite at the nuclear waste disposal site in Olkiluoto, Western Finland. *International Journal of Rock Mechanics and Mining Sciences*, *79*, 135-148.

Skyttä, P., Ovaskainen, N., Nordbäck, N., Engström, J., & Mattila, J. 2021: Fault-induced mechanical anisotropy and its effects on fracture patterns in crystalline rocks. *Journal of Structural Geology*, *146*, 104304.

Smith, M. W., Carrivick, J. L., & Quincey, D. J. 2016: Structure from motion photogrammetry in physical geography. *Progress in Physical Geography*, *40*(2) 247-275.

Sun, C., & Pallottino, S. 2003: Circular shortest path in images. *Pattern Recognition*, *36*(3), 709-719.

Tchalenko, J. S. 1970: Similarities between shear zones of different magnitudes. *Geological Society of America Bulletin*, *81*(6), 1625-1640.

Tchalenko, J. S., & Ambraseys, N. N. 1970: Structural analysis of the Dasht-e Bayaz (Iran) earthquake fractures. *Geological Society of America Bulletin*, *81*(1), 41-60.

Thiele, S. T., Grose, L., Samsu, A., Micklethwaite, S., Vollgger, S. A., & Cruden, A. R. 2017: Rapid, semi-automatic fracture and contact mapping for point clouds, images and geophysical data. *Solid Earth*, *8*(6), 1241-1253.

Vermilye, J. M., & Scholz, C. H. 1998: The process zone: A microstructural view of fault growth. *Journal of Geophysical Research: Solid Earth*, *103*(B6), 12223-12237.

Vincent, L. 1998: Minimal path algorithms for the robust detection of linear features in gray images. *Computational Imaging and Vision*, *12*, 331-338.

Vollgger, S. A., & Cruden, A. R. 2016: Mapping folds and fractures in basement and cover rocks using UAV photogrammetry, Cape Liptrap and Cape Paterson, Victoria, Australia. *Journal of Structural Geology*, *85*, 168-187.

Wellington, S. L., & Vinegar, H. J. 1987: X-ray computerized tomography. *Journal of Petroleum Technology*, *39*(08), 885-898.

Weng, X., Kresse, O., Cohen, C. E., Wu, R., & Gu, H. 2011, January: Modeling of hydraulic fracture network propagation in a naturally fractured formation. In *SPE Hydraulic Fracturing Technology Conference*. Society of Petroleum Engineers.

Withjack, E. M. 1988: Computed tomography for rock-property determination and fluid-flow visualization. *SPE formation evaluation*, *3*(04), 696-704.

Woodcock, N. H., & Schubert, C. 1994: Continental strike-slip tectonics. In *Continental deformation* (pp. 251-263).

Xu, S., & Ben-Zion, Y. 2013: Numerical and theoretical analyses of in-plane dynamic rupture on a frictional interface and off-fault yielding patterns at different scales. *Geophysical Journal International*, *193*(1), 304-320.

Özkaya, S. I. 2003: Fracture length estimation from borehole image logs. *Mathematical Geology*, *35*(6), 737-753.

Appendix 1. Problems related to grinding tomography process and solutions

Use of GNR16 3D-grinder was at developmental stages at the start of this Thesis. The time consumed for this working stage was approximately 200 hours. Development and testing of the method took around 40 hours and 160 hours for the grinding process, which both acquired constant supervision.

In order to start the grinding process, the vacuum had to be reached and maintained at an acceptable level +90. To reach the desired level, the sample table, stainless steel rim and the glasses had to cleaned with intense care, as any impurity might have caused problems reaching the desired level of vacuum. In addition, the steel rim and sample glasses had to be placed very carefully to avoid any kind of material that could be removed when the steel rim or samples hit the sample table. In cases where the vacuum wasn't reached, the cleaning and sample placing had to be done again, if this process failed several times, it sometimes took over an hour to reach acceptable vacuum level. Furthermore, gluing the samples on 3 mm thick glass sheets also caused problems with reaching desired vacuum levels, as the glasses tend to curve a bit while the glue is drying, causing imbalance between the glass sheet and the sample table and the vacuum levels stayed low. The problem was solved by using double 3 mm thick glass sheets, after which the glasses maintained perfectly flat and the desired vacuum level was reached.

In the start of the process after vacuum is reached, the machine detects sample surface and afterwards software starts identifying the samples with the camera, from the sample table by rotating it 12 degrees at a time. Occasionally the software was unable to detect samples from the table and was bugged; the process had to be re-started over again. When samples were successfully identified, the actual grinding process started. Sample identifying problems were also randomly encountered after the 1st grinding cycle was finished. Occasionally, the software was not able to recognize the photographed sample, which resulted in re-starting the process again. A less harm causing problem was associated with the same type of identification problems, when, the camera was unable to target the sample properly but despite this, the software photographed the sample and the process continued (Fig. 24). These problems appeared to be related to the colour contrasts and moisture of the sample surface, and reflections of light, caused by water laying on the sample table, in addition to possible crooked samples. Other photographic problems were linked to pressurized air flow and sample surface wetness. As the samples were porous enough, they initially dried up, due to too high airflow. As the pressurized air flow

was adjusted for a lower flow, sample surfaces were disturbed by the lubricant water, causing bad quality photographs (Fig. 25). Even at minimum air flow, samples from Geta dried up completely while photographing (Fig. 26). The problem was solved temporarily by attaching a piece of dishrag to the roof part of the machine, whereby the dishrag cleaned the sample surface from splashes and dirt in each round, as well as kept it moist for photography.

The grinding process was conducted at a feed rate of 20-100 microns / min with diamond wheel type 140. The feed rate had to be adjusted according to the torque (Nm), as the diamond wheel started to get clogged, the Nm value of machine applying force to the sample surface rose, as it had to apply higher force in order to grind the sample as the wheel was clogged. The machine had a security limit of 1.5 Nm, which, when exceeded, stops rotating the table, without stopping the wheel spin, which rotates at set level (2000 rpm), potentially damaging the accuracy of the device, therefore the machine acquired constant supervision. High torque values were caused by either three different reasons, as well as their combinations: 1. Defected diamond wheel appeared to be most notable affecting reason for high torque values. 2. The hardness of the sample effect on the values considerably; Rapakivi samples from Geta, Åland, appeared to be harder, causing higher torque values, than the corresponding samples from Orrengrund, Loviisa. 3. Clogged wheel was the least affective; although the wheel was always removed when increased Nm values were detected. Eventually, as grinding work progressed, it was found that the diamond wheel was defective and therefore, changed to another, which allowed usage of 100 microns / min at best, even though it appeared that the wheel gets clogged too fast at this feed rate in order of rational grinding time. After testing, the suitable feed rate found out to be 50-70 µm / minute, at this rate the process had to be paused in approximately every 2-3 hours so that the wheel could be removed and opened by grinding the diamond wheel with a sanding stick.

High Nm values affected, in addition to loading of the machine, to the accuracy of the grinded intervals. As the desired grinding depth per cycle was set to 50 microns, high torque values together with the aforementioned problems, caused variation of +25 micron to the grinding accuracy. When the diamond wheel was freshly opened and feed rate set at around 50 microns, the accuracy varied only for +5 µm, yet it climbed up comparatively fast. The average grinded interval in this Thesis appeared to be 70 µm instead of 50 µm, having no effect on the accuracy when observed with the naked eye.

Additionally, other problems that are encountered with machine are related to its user.Every set parameter should be double checked before turning on the process.

In this project/thesis, possible solutions were partially developed for recognized problems in grinding tomography method pointed out by Pascual-Cebrian et al. (2013) e.g. constant lighting-condition on sample, automatic picture data alignment. Most of the difficulties are simply technical issues that can be easily fixed.

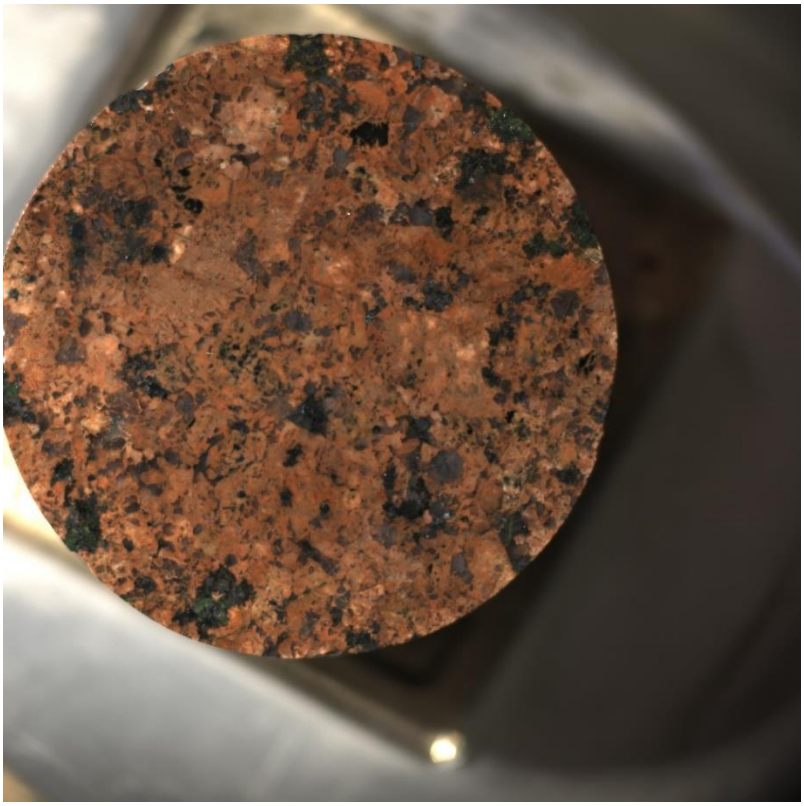

Figure 24: Camera unable to target the sample properly but despite this, the software photographed the sample.

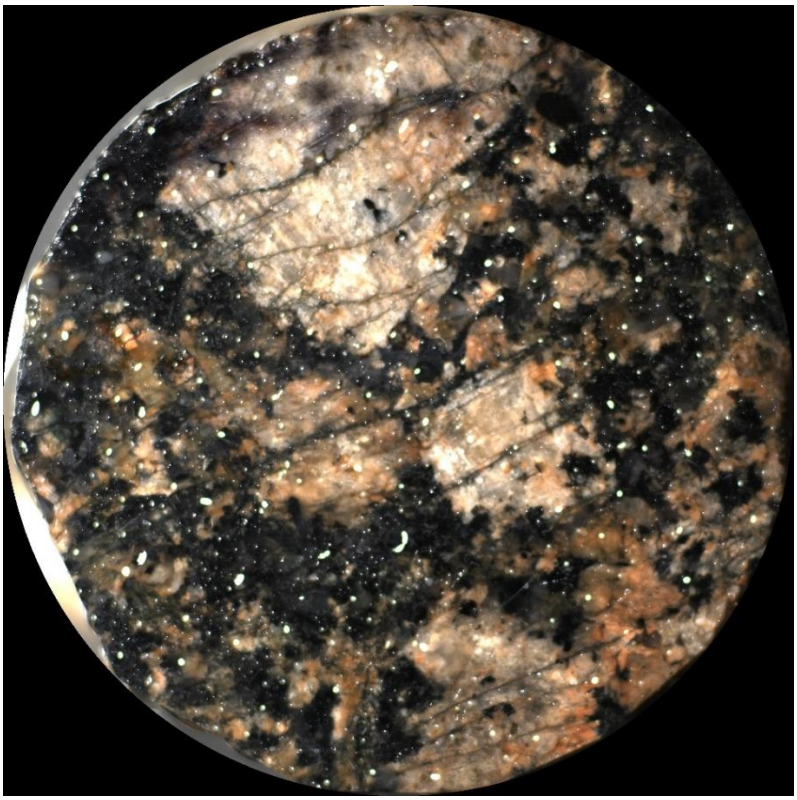

Figure 25: Sample surface disturbed by the lubricant water.

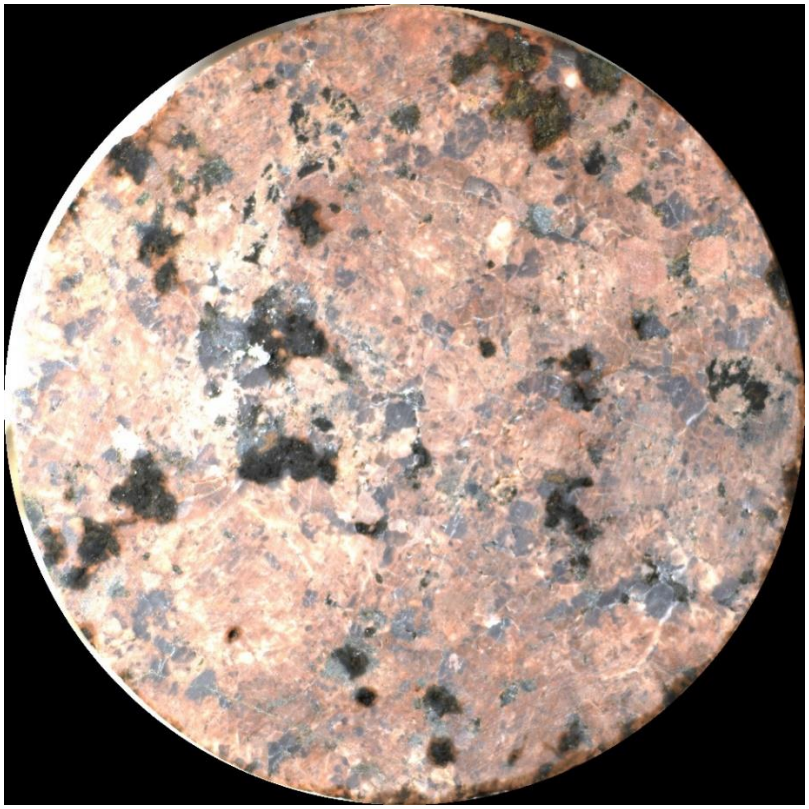

Figure 26: Air flow dried up the sample completely while photographing.